Ceramics International xxx (xxxx) xxx

Contents lists available at ScienceDirect

Ceramics International

journal homepage: www.elsevier.com/locate/ceramint

Review article

Assessing Mn as an antioxidant agent in bioactive glasses by quantification of catalase and superoxide dismutase enzymatic mimetic activities

Matteo Abati [a,c], Altair T. Contreras Jaimes [b,c], Luca Rigamonti [a], Debora Carrozza [a], Gigliola Lusvardi [a], Delia S. Brauer [c,**], Gianluca Malavasi [a,*]

[a] Department of Chemical and Geological Sciences, Università degli Studi di Modena e Reggio Emilia, via G. Campi 103, 41125, Modena, Italy
[b] Fraunhofer-Institut für Silicatforschung (ISC), Neunerplatz 2, 97082, Würzburg, Germany
[c] Otto Schott Institute of Materials Research, Friedrich Schiller University Jena, Fraunhoferstr. 6, 07743, Jena, Germany

ARTICLE INFO

Handling Editor: Dr P. Vincenzini

Keywords:
Catalase mimetic activity
Bioactive glasses
Manganese
Superoxide dismutase
Apatite

ABSTRACT

The antioxidant activity of Mn as additive in a 45S5 type glass system with and without P_2O_5 was studied by mimicking the activity of catalase (CMA) and superoxide dismutase (SOD) enzymes. Glasses were melted either under oxidizing or reducing atmosphere (N_2/H_2) to compare the processing influence on the Mn oxidation state. Thermal (DTA) and optical (UV–Vis) characterizations of the glass powders were carried out to obtain further insight into the structural role of Mn. A correlation of *in vitro* apatite formation between Tris buffer solution and Simulated Body Fluid (SBF) was performed to optimise Mn substitution, where a decrease in apatite formation was observed by increasing Mn content. Despite this, glasses with up to 1.0 mol% MnO did not show any delay in apatite formation and maintained their CMA and SOD activity. The antioxidant effect of Mn can be attributed to the interconversion $Mn^{2+} \leftrightarrow Mn^{3+}$ occurring on the glass surface through a heterogeneous catalysis. P_2O_5 plays an important role in the antioxidant effect of the glass, possibly by charge balancing Mn ions and forming more stable units compared to those formed with Ca and Na. The amount of Mn^{2+} is predominant in the glass network with respect to Mn^{3+} in all synthetized glasses. Moreover, glass melting in a reducing atmosphere further avoided Mn oxidation.

1. Introduction

The implantation of biomaterials to treat and repair tissues has inherent inflammatory and repair mechanisms. During these processes, redox reactions occur and cells such as platelets and macrophages release reactive oxygen species (ROS). With this regard, the effect of oxidative stress in biomaterials has been overlooked despite the influence of the chemical composition, surface properties and by-products being of importance in the production of oxidant molecules. Furthermore, low levels of oxidative stress can lead to a low immunological response and infections while high levels are associated with implant rejection [1].

It has been investigated that an *in vitro* decrease in superoxide-dismutase (SOD) enzymes after exposure to Ti6Al4V implants, with high ROS levels such as superoxide anion (O_2^-), was associated with pathological events after implantation of coronary artery stents. Additionally, pre-existing inflammation in the host tissue was reported to be an affecting factor of the redox balance and tissue repair [1].

As the first biomaterial to be considered bioactive, Bioglass® 45S5 [2,3] has extensive potential applications owing to the multiple options in which its glass network can be modified, by means of doping with alkaline, alkaline earth and transition metal ions [4,5]. It has been proved that one of the main factors controlling the composition-degradation relationship is the silicate network connectivity (NC) given by its chemical composition [6,7]. Consequently, the glass dissolution mechanism plays a key role in its bioactivity, allowing for tissue regrowth and actively stimulating cells to produce new tissue. During the first few hours of contact in a biological environment, a complex mechanism of alkaline ions release occurs. The exchange of these ions with H^+ from the surrounding aqueous solution leads to the formation of the initial reaction film, which evolves into a silica-gel layer and consecutively into a mineralized hydroxyapatite layer [2].

The incorporation of functional ions in the glass structure has shown to improve their physical and therapeutic properties by adapting their

* Corresponding author.
** Corresponding author.
E-mail addresses: delia.brauer@uni-jena.de (D.S. Brauer), gmalavasi@unimore.it (G. Malavasi).

https://doi.org/10.1016/j.ceramint.2023.10.091
Received 12 June 2023; Received in revised form 18 September 2023; Accepted 10 October 2023
Available online 11 October 2023

chemistry depending on the final application. These effects are associated with antibacterial activity (Ag [8–11] and Ga [12,13]), stimulation of bone development and maintenance (Mg [14], Sr [15], Zn [16,17], and Co [18]), fluorapatite precipitation (F [19–21]), mechanical properties (K [22,23]), reduction of local oxidative stress (Ce [24], Sr [25]), and in magnetic localised hyperthermia for tumours treatment (Fe [26]).

Amongst the different ions with therapeutic properties, Mn has attracted attention in recent years for incorporation in different bioceramics [27–29]. Recent works highlight advantages of glasses doped with Mn compared to other materials doped, for example, with Mg [30], Sr[29], Ag [31], Te [32] or Se [33]. The incorporation of Mn into bioactive glasses synthesized by melt [34,35] or sol-gel [36–39] routes, were done because Mn has an important role in relevant biological processes. As a redox-active metal, Mn is important in the oxygen chemistry within the body by acting as a catalytic cofactor for SOD metalloenzymes, which remove toxic products from O_2 metabolism such as superoxide (O_2^-) and hydrogen peroxide [40]. Mn also acts as a mediator of interactions between cells and the surrounding environment, and as an activator of integrins and glycoproteins of the cellular membrane [41].

Concerning the clinical applications of bioactive glasses, it is known that Mn plays an essential role in key cellular processes involved in the metabolism of hard tissues [4,42], such as: extracellular matrix remodelling (ECM) [43], improvement of bone mineralization [37,44], cell adhesion, proliferation [45] and bone mass maintenance [46]. Therefore, further research dealing with its potential use in clinical applications in bone regeneration is of great interest. For example, incorporation of small amounts of Mn in bioactive silicate glasses showed positive effects such as *in vitro* osteoblast growth and osteogenic activity [39,47]. A previous study on CMA activity of a series of doping ions [48] showed that Mn had the highest decomposition rate (k) after Co, with other tested ions being Cu > Ce > Fe > V > Ti > Zr. Similarly, Kapoor et al. [39] found that a 1 mol% MnO doping in a bioactive type glass showed the best outcome when tested under oxidative stress conditions among other ions (Co, Cu, Fe) [39]. The antioxidant activity was also described to be dose-dependant [39] with its effect being gradually reduced up to a 5 mol% content in a bioactive type glass. In view of these results, a more detailed to study on Mn-containing potential bioactive glasses is very important to find the best compositions for obtaining glasses with bioactivity and CMA.

The significance of adjusting Mn concentration is also fundamental since more than 1 mol% of MnO_2 was reported to have a negative effect on bioactivity for 45S5 containing glasses [35]. However, the confirmation for this trend should be further investigated, since this study by Srivastava et al. [35] substituted MnO by CaO on a weight basis instead of a molar basis. While Ca and Mn have comparable charge/size ratio, leading to the hypothesis that Mn^{2+} acts also as a modifier ion [34,36,49], substitution in wt.% was reported to lead to significant changes in the glass dissolution because of structural modifications [50].

The substitution of Ca^{2+} with Mn^{2+} was previously reported to maintain the glass NC, since both are divalent ions [51] and therefore should have a comparable effect on the bioactivity [36]. Moreover, during the melting process, a portion of the Mn^{2+} ions can be oxidized to Mn^{3+} [52–54], and the coexistence of Mn in two oxidation states, as Mn^{2+} [34,37] or as Mn^{3+} [55], can lead to variation in properties such as coordination number, ligand field strength and optical absorption.

Therefore, the aim of this work is to substitute Ca^{2+} by Mn^{2+} in increasing quantities up to 4 mol% MnO. The glass systems are based on the 45S5 glass (46.1 SiO_2 - 24.4 Na_2O - 26.9 CaO - 2.6 P_2O_5 mol% [5]) and its phosphate free counterpart (called N25C25S50 glass), as described by Kokubo and co-workers (50 SiO_2 - 25 Na_2O - 25 CaO mol%) [56]. In addition, the influence of glass synthesis in a reducing atmosphere is evaluated with particular emphasis given to the structural role of Mn^{2+}/Mn^{3+} and the correlation between glass composition and *in vitro* bioactivity. The antioxidant activity is assessed by quantification of CMA and SOD enzymes.

2. Materials and methods

2.1. Glass synthesis

Table 1 shows the melt-derived bioactive glass series modified by molar substitution of CaO for MnO (0.5, 1.0, 2.0 and 4.0 mol%) produced in oxidizing (air) and reducing (N_2/H_2) atmospheres. Glasses were prepared by mixing SiO_2 (>99.0%), Na_2CO_3 (>99.0%), $CaCO_3$ (>99.0%), $NaPO_3$ (pure grade) and $MnCO_3$ (>99.5) all from Carl Roth, Germany. 45S5 based glasses are labelled as "H *x*Mn" while the phosphate free series are labelled as "K *x*Mn", where *x* is the MnO content in mol%. For each composition, raw materials were weighed and mixed with the aid of alumina balls before being transferred into a Pt crucible and covered with a Pt lid. A preheating step at 600 °C for 30 min was carried out to avoid foaming, after which the glass was melted at 1340 °C for 1 h. The melt was then water-quenched to obtain a frit and dried in an oven at 100 °C overnight. Glass powders were obtained by grinding the frit with an agate pestle. The powders were sieved to a particle size range between 125 and 250 μm and stored in a desiccator until further use.

In addition, a selection of Mn-containing bioactive glasses based on compositions 45S5 (0.5 or 1.0 mol% MnO) and N25C25S50 (1.0 mol% MnO) were prepared by melting in a reducing atmosphere (N_2/H_2 90:10) within an electric furnace to avoid oxidation of Mn^{2+} to Mn^{3+} at 1340 °C for 1 h. Melts were quenched onto a block using a graphite stamp to obtain samples. The samples are named as "H *x*Mn_red" or "K *x*Mn_red". Samples with 1 mol% MnO (H 1.0Mn_red and K 1.0Mn_red) were not visually homogeneous, probably owing to partial crystallization during the melting process, as confirmed by XRD. Hence, these were not processed further.

2.2. Chemical characterization

Compositional analysis of the glass powders (125–250 μm size range) was performed by X-ray fluorescence (XRF) spectroscopy with a PW 1480 instrument (Philips, Netherlands). Argon methane mix was used as the inert gas. An error of <0.7% was calculated after quantitative analysis obtained from calibration with silicate references containing Mn.

Thermal analysis was performed by differential scanning calorimetry (DSC) with a PT-1600 instrument (Linseis, Germany). Glass powders (90 mg/125–250 μm) were heated at 10 °C/min in a platinum crucible in two steps: from RT to 580 °C, cooling down to 150 °C, followed by heating up to 1000 °C. All measurements were corrected with a background analysis carried out with an empty platinum crucible.

Temperature-Programmed Reduction (TPR) is a characterization technique widely used to determine the reduction properties of bulk and/or supported metal oxides as temperature is linearly increased in a

Table 1
Experimental composition (mol%) of the synthesized samples obtained by XRF analysis and nominal values (in parenthesis). An error <0.7% was calculated from calibration curves.

Glass	SiO_2	Na_2O	CaO	P_2O_5	MnO
H	46.3 (46.1)	24.1 (24.4)	27.1 (26.9)	2.5 (2.6)	–
H 0.5Mn	46.3 (46.1)	24.1 (24.4)	26.5 (26.4)	2.6 (2.6)	0.5 (0.5)
H 1.0Mn	46.3 (46.1)	24.1 (24.4)	26.1 (25.9)	2.5 (2.6)	1.0 (1.0)
H 2.0Mn	46.2 (46.1)	24.0 (24.4)	25.2 (24.9)	2.6 (2.6)	2.0 (2.0)
H 4.0Mn	45.6 (46.1)	24.5 (24.4)	23.3 (22.9)	2.6 (2.6)	4.0 (4.0)
K	50.0 (50.0)	25.6 (25.0)	24.4 (25.0)	–	–
K 0.5Mn	49.9 (50.0)	25.4 (25.0)	24.2 (24.5)	–	0.5 (0.5)
K 1.0Mn	49.9 (50.0)	25.4 (25.0)	23.8 (24.0)	–	0.9 (1.0)
K 2.0Mn	49.9 (50.0)	25.2 (25.0)	22.9 (23.0)	–	2.0 (2.0)
K 4.0Mn	49.8 (50.0)	24.9 (25.0)	21.3 (21.0)	–	4.0 (4.0)
H 0.5Mn_red	46.5 (46.1)	24.2 (24.4)	26.1 (26.4)	2.7 (2.6)	0.5 (0.5)
H 1.0Mn_red	45.4 (46.1)	24.6 (24.4)	26.1 (25.9)	2.8 (2.6)	1.1 (1.0)
K 1.0Mn_red	48.5 (50.0)	25.9 (25.0)	24.5 (24.0)	–	1.1 (1.0)

reducing flow. TPR analyses are usually carried out using a standardized experimental protocol and conditions such as solid mass, flow rate, reducing/oxidizing concentration and heating rate [57]. In particular, this technique was reported to successfully investigate the $MnO_2 \rightarrow MnO$ reduction on bulk manganese oxide catalysts [58].

In this study H_2-TPR was conducted in a ChemiSorb 2750 (Micromeritics, USA) equipped with a thermal conductivity detector (TCD). The glass powder (250 mg, 125–250 μm) was placed in a quartz reactor, degassed at 200 °C under a 20 mL/min N_2 flow and reduced under a 20 mL/min H_2/N_2 (10% *v/v*) flow at a heating rate of 10 °C/min from RT up to 900 °C. The TCD signal was then converted to concentration of active gas (H_2) using a level calibration. The H_2 consumption was calibrated using TPR of Ag_2O at the same experimental conditions. The fraction of Mn^{3+} is calculated according to (1):

$$Mn^{3+}/Mn_{total}(\%) = (H_2(mmol/g)*2/(Mn_{total}(mmol/g))*100 \quad (1)$$

While the occurring, chemical reaction is represented by:

$$2\ Mn^{3+} + H_2 \rightarrow 2\ Mn^{2+} + 2H^+$$

X-ray diffraction (XRD) analyses were performed on crystallized glass samples obtained performing a thermal treatment (2 h) at crystallization temperature (T_c) on glass sample powders. The measures were done using a Panalytical X'Pert Pro XRD (Malvern Panalytical, Netherlands), with Ni-filtered Cu Kα radiation (λ = 1.54060 Å). A generator voltage of 40 kV and a tube current of 40 mA was employed. The conditions for data collections were $20 < 2\theta < 60°$ range and step size 0.033°. X-ray diffraction patterns of the glasses before and after immersion in Tris buffer solution and SBF were collected using the same instrument. Diffraction patterns were collected at RT in the 15–55° 2θ range, with a step size of 0.033°.

Infrared spectra of all glasses were collected using attenuated total reflection (ATR) Fourier transform infrared spectroscopy (FT-IR; Agilent Cary 630 ATR FT-IR Spectrometer, Agilent Technologies GmbH, Germany), to qualitatively characterize the glass structure before and after immersion in Tris buffer solution and SBF to detect apatite formation. The spectra were collected from 4000 to 400 cm^{-1} with a 2 cm^{-1} resolution and 32 scans per measurement.

Optical absorption spectra of all glasses were recorded in the 250–650 nm range (JASCO V-570 double-beam UV–Vis–NIR spectrophotometer, JASCO, USA) with the implementation of a 60 mm integrating sphere element (JASCO, USA) required for analysis on glass powders. This technique was used to qualitatively characterize the Mn oxidation state when incorporated in the glasses and to analyse its redox behaviour during glass immersion in H_2O_2 for catalase mimetic activity (CMA).

2.3. Immersion studies

In vitro bioactivity was evaluated in SBF and Tris buffer solutions, with both being prepared following a protocol described in the literature [59]. The immersion tests were carried out by soaking 75 mg of glass powders (125–250 μm, 3 independent replicates) in 50 mL of SBF solution or 0.062 mol/L tris(hydroxymethyl)aminomethane-HCl buffer solution (Tris buffer) for 1, 4, 7, 14 and 28 d. Samples were maintained in a shaking incubator at 37 °C at 60 rpm before filtering [60]. Blank samples consisting of 50 mL of either of these solutions were used as controls. The elemental concentration of the ions released into Tris buffer solution at each time-point was obtained by inductively coupled plasma optical emission spectroscopy (ICP-OES Varian Liberty 150, Agilent Technologies, Germany). XRD and ATR FT-IR spectroscopy were used to identify the presence of apatite on the glass surface after immersion.

pH measurements were performed using a portable pH-meter SevenGo Starter-Kit SG2-ELK (Mettler-Toledo, USA) calibrated before each set of measurements using pH 7.01 and 10.01 standard solutions (Hanna Instruments, Germany).

2.4. Antioxidant activity

The antioxidant activity of the glasses was measured by their CMA and SOD mimetic activity. The CMA method has been previously described in detail [25], and was performed by soaking 100 mg of glass powder (125–250 μm, n = 3) in 20 mL of H_2O_2 1 mol/L and maintained on a shaking plate at 37 °C and 60 rpm. H_2O_2 1 mol/L blank solutions were measured at each time-point (1, 4 and 7 d) to normalise results considering the spontaneous degradation of H_2O_2. The antioxidant activity for each glass was determined by quantification of the peroxide residue in solution through permanganatometric titration (n = 2).

Conversely, the SOD method is not standardized for bioactive glasses, and therefore a previously reported procedure developed by Ukeda et al. [61] was adapted in two different protocols to understand whether the catalytic decomposition of $O_2^{\bullet-}$ anions occurs homogeneously in solution or heterogeneously on the glass surface. The first procedure is referred as "homogeneous" because the potential enzymatic activity originates from the species released from the glass into deionized water during the incubation step. This protocol consists of placing 100 mg of glass powder (125–250 μm) into a 15 mL PP centrifuge tube (Sigma-Aldrich, Italy) with 5 mL of deionized water. The centrifuge tube was kept in a shaking incubator at 37 °C and 120 rpm for 1 h. Afterwards, the tube was centrifuged at 1000 rpm for 10 min and the supernatant was filtered using a 0.45 μm Acrodisc® syringe filter (Sigma-Aldrich, Italy), and then used for the SOD test as proposed by the measurement kit (19160 SOD determination kit, Sigma Aldrich). The second protocol is referred as "heterogeneous" because the potential enzymatic activity originates directly from the glass bulk. The test was carried out by placing 50 mg of glass powder (125–250 μm) and using it directly with the measurement kit as per manufacturer instructions. After each procedure, optical absorption was measured using UV–Vis spectrophotometry (JASCO V-570, USA) and the inhibition rate % (I.R. %) was calculated to quantify SOD activity [62].

Statistical analysis was performed using OriginPro2019 Statistics App. One-way analysis of variance (ANOVA) and Bonferroni multiple comparisons was used with $p < 0.05$ defined as the level of statistical significance.

3. Results

Glassy materials were obtained for both series (H *x*Mn and the K *x*Mn), and substitution of Ca by Mn gave a purple-like tone to the glasses, with colour intensity increasing with Mn content. This was associated with the presence of Mn^{3+} ions [63], owing to the $MnCO_3$ decomposition. The thermal process occurs via various steps [64], with Mn^{2+} being the stable redox state above 1030 °C. However, an incomplete decomposition of Mn_3O_4 to MnO may explain the presence of Mn^{3+} ions. In contrast, a yellow tone was observed for one of the glasses melted in reducing atmosphere (H 0.5Mn_red), supporting the avoided oxidation of Mn^{2+}. Samples with higher Mn content (H 1.0Mn_red and K 1.0Mn_red) were not completely transparent and visually not homogeneously in colour when melted in a N_2/H_2 atmosphere. This was associated with the partial crystallization of the glasses, which was later confirmed by XRD.

The experimental compositions of all synthesized glasses analysed by XRF agree with the nominal ones (Table 1).

The effect of Mn^{2+} ions on the glass colour was analysed by UV–Vis spectroscopy (Fig. 1). As reported in the literature for other silicate glasses [65,66], Mn^{2+} has a weak absorption band at around 415–430 nm corresponding to the spin-forbidden $^6A_1 \rightarrow {}^4A_1$ transition that confers the pale-yellow colour. By contrast, Mn^{3+} presents an absorption band at around 470–500 nm, corresponding to the $^5Eg \rightarrow {}^5T_{2g}$ transition, which is about one-hundred times more intense than the Mn^{2+} band and confers the purple colour. Fig. 1 shows the UV–Vis spectra for all the

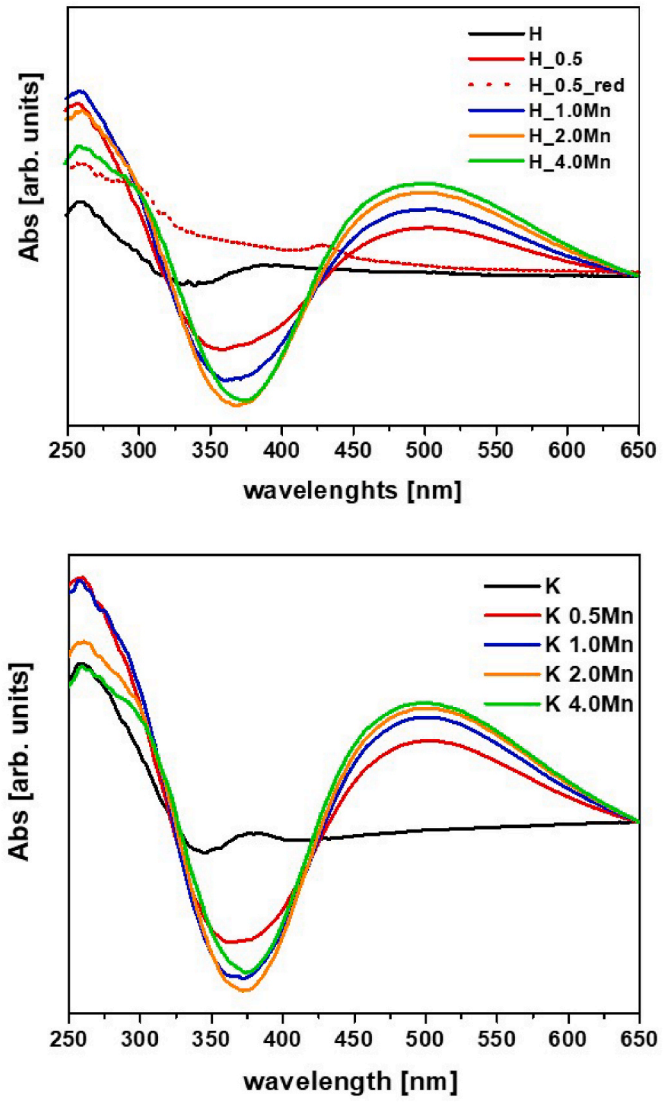

Fig. 1. Total reflectance UV–Vis spectra of glass powders with increasing Mn content upper panel: H *x*Mn; bottom panel: K *x*Mn.

glasses, where the main band in the visible region is positioned at 500 nm and it is assigned to Mn^{3+}. However, the weak band positioned at 430 nm, corresponding to Mn^{2+}, was detected for the 45S5 glass with 0.5 Mn mol% produced in a reducing atmosphere. Therefore, we could consider that in both glass series the Mn^{3+} band, by having a higher absorption coefficient, overlaps and disguises the Mn^{2+} signal [66].

In this study, the H_2-TPR technique was implemented to characterize the oxidation state of Mn [67]. For this, XPS was used to provide surface related information, while H_2-TPR also provided bulk related information. A study on Ce containing bioactive glasses pointed out that XPS characterization only showed evidence of a surface occurring reaction between the powder and the H_2O_2 solution [24].

Hence, in this study we have chosen to characterize by H_2-TPR the glasses with the higher Mn content (H 4.0Mn and K 4.0Mn) and their Mn free versions. Fig. 2a shows the H_2-TPR profile for H4.0Mn and K4.0Mn glasses. The final H_2-consumption (mmol/g) was determined as the difference between the redox behaviour of the glasses with and without MnO. Therefore, it was possible to obtain the value that exclusively corresponds to the effect of MnO in the glass composition. This analysis showed that the change in oxidation state occurs between 200 and 700 °C. H_Mn showed the highest H_2 consumption with two peaks at 270 and 350 °C, suggesting that the presence of P_2O_5 in the glass composition induces a higher fraction of Mn^{3+} when compared with K_4.0Mn.

The temperature range of Mn^{3+} reduction (200–700 °C) is slightly higher with respect to that found for Mn_2O_3 in the literature [68]. This was associated with the amorphous character of the studied materials. The calculated fraction of Mn^{3+} was 10% for H 4.0Mn and 5% for K 4.0Mn, assuming that the H_2-consuption is due to the complete reduction of Mn^{3+} to Mn^{2+}. This result was confirmed by the UV–Vis analysis performed after H_2-TPR (Fig. 2b). Here, an intensity reduction of the 500 nm Mn^{3+} absorption band was observed. Moreover, the Mn^{2+} spin-forbidden transition band at 430 nm also appears to be a weak band.

Figure S1a, S1b and Fig. 3a show the XRD patterns of the glasses, confirming their amorphous character (H *x*Mn and K *x*Mn), and therefore that Mn was successfully incorporated in the glass network. Conversely, the samples melted in a reducing atmosphere (H 1.0Mn_red and K 1.0Mn_red) were partially crystallized to $Na_2CaSi_2O_6$[69] (Fig. 3a–b). Since it was not possible to obtain glassy samples for these compositions, no further characterization was carried out owing to the differences in ion release that result from partially crystallized samples when compared with their glass counterpart [70,71].

Fig. 4 shows the DSC curves for the H *x*Mn and K *x*Mn glasses. The general trend of decreasing T_g with increasing Mn content was observed for both series. Nonetheless, this effect was not considered within the K

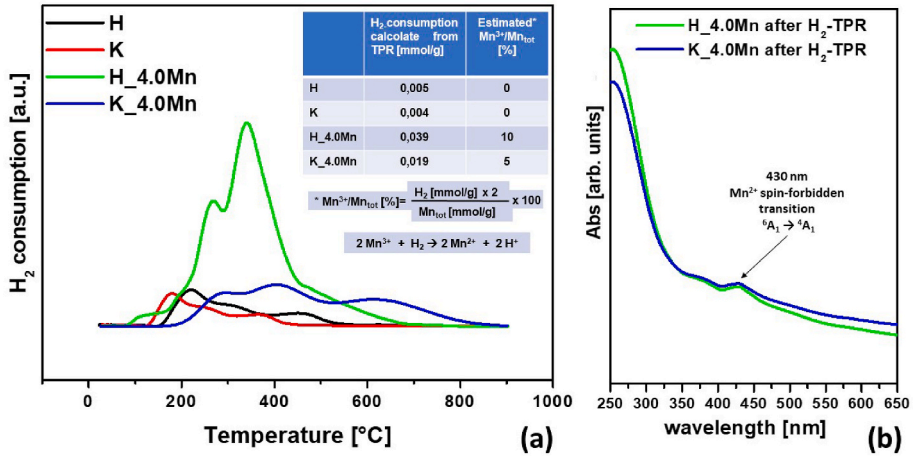

Fig. 2. (a) H_2-TPR profile measured between 25 and 900 °C for H and K glass series with and without Mn (4 mol%). (b) Total reflectance UV–Vis spectra after H_2-TPR analysis of Mn containing glasses H 4.0Mn and K 4.0Mn.

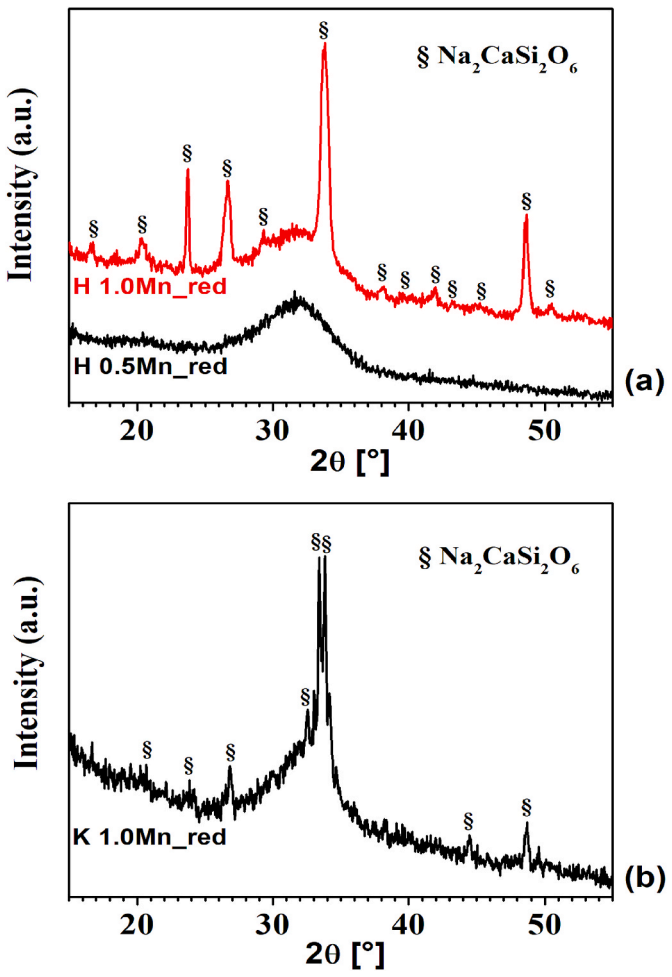

Fig. 3. (a) XRD powder patterns of H 0.5Mn_red and H 1.0Mn_red glasses, and (b) K 1.0Mn_red glass; (§) = $Na_2CaSi_2O_6$. (For interpretation of the references to colour in this figure legend, the reader is referred to the Web version of this article.)

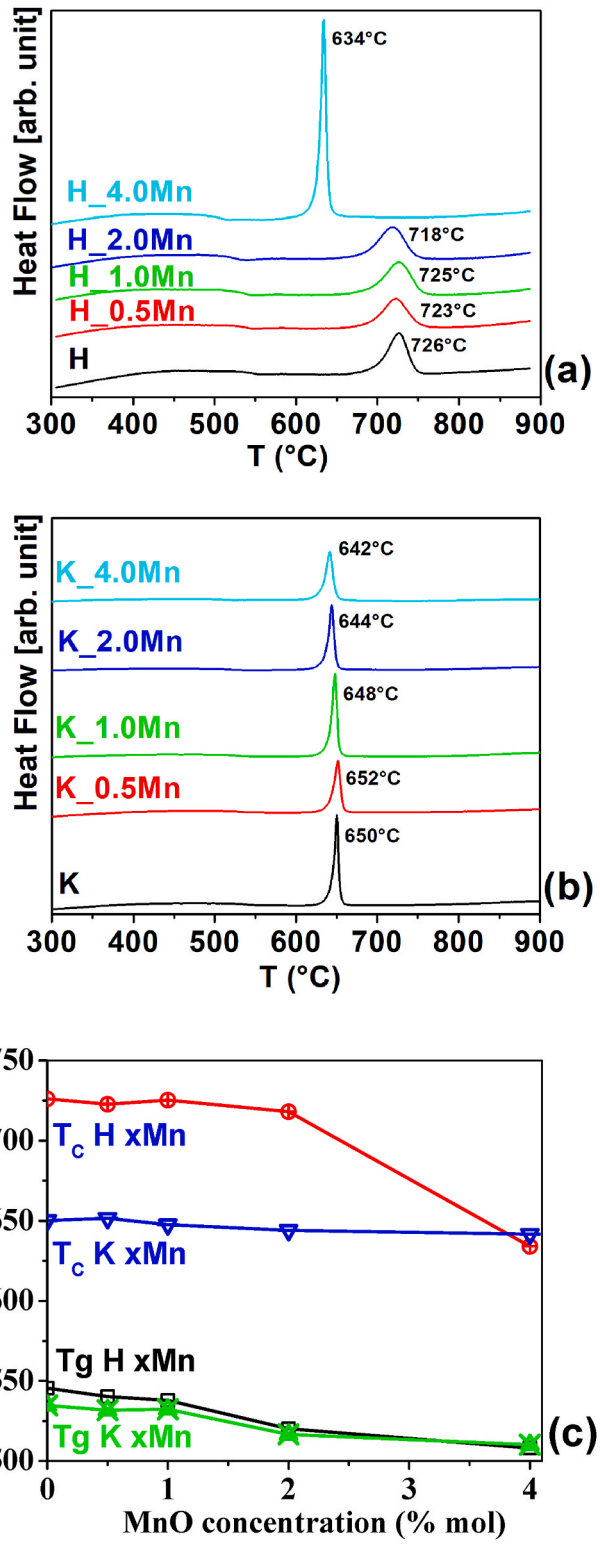

Fig. 4. DSC curves showing crystallization temperature (T_c) of glasses (a) H *x*Mn and (b) K *x*Mn glass series. (c) Glass transition (T_g) and crystallization temperatures (T_c) as a function of MnO concentration.

series varying up to 1.0 Mn mol% since differences would fall within the instrumental error. Even if both Mn^{2+} and Mn^{3+} act as modifier ions [34,37,49], but with differ effect on glass network. The substitution of Ca^{2+} with Mn^{3+} leads to lower network connectivity, because of the formation of larger numbers of non-bridging oxygens (NBOs), which can be expected to cause a decrease of T_g. However, Mn^{3+} can also be expected to form stronger bonds to oxygen compared to Ca^{2+} or Mn^{2+} (bond strength z/a, Mn^{3+} (coord. 6) = 1.50 *vs* Mn^{2+} (coord. 6) = 0.92 and Ca^{2+} (coord. 6) = 0.85 [72]), and this can be expected to increase T_g. In average, this value was higher for P_2O_5 free glasses with Mn content up to 1 mol%. This difference was associated to its NC (2.00 vs. 2.12) leading to a less cross-linked structure. The addition of P_2O_5 re-polymerises the silicate network as Ca and Na have a higher affinity with the phosphate groups [73].

For both the H *x*Mn and K *x*Mn glass series, crystallization temperature (T_c) did not significantly change with Mn content, except for H 4.0Mn, which showed a lower T_c. One possible explanation could be that glasses with up to 2 mol% of MnO crystallise to comparable phases, whereas the decrease of T_c at 4 mol% MnO in the H xMn glass series may indicate that a different crystalline phase is formed, or that an interaction with the phosphate phase occurs. In general, the T_c of the H *x*Mn series is higher than T_c of the K *x*Mn series, owing to the presence of the phosphate phase that increases the disorder in the network and, thus, hinders the mobility of ions to form crystals. This observation was confirmed by XRD analysis performed on H 2.0Mn, H 4.0Mn and K4.0Mn glassy powder after thermal treatment at T_c, respectively, for 2 h. The introduction of 4.0% of MnO in the H system promoted the formation of the crystal phase β-$NaCaPO_4$ (Fig. 5).

The processing window (T_c–T_g) is larger for the phosphate containing glasses (H *x*Mn) resulting in reduced tendency to crystallise when compared with the K *x*Mn series, making synthesis and further glass

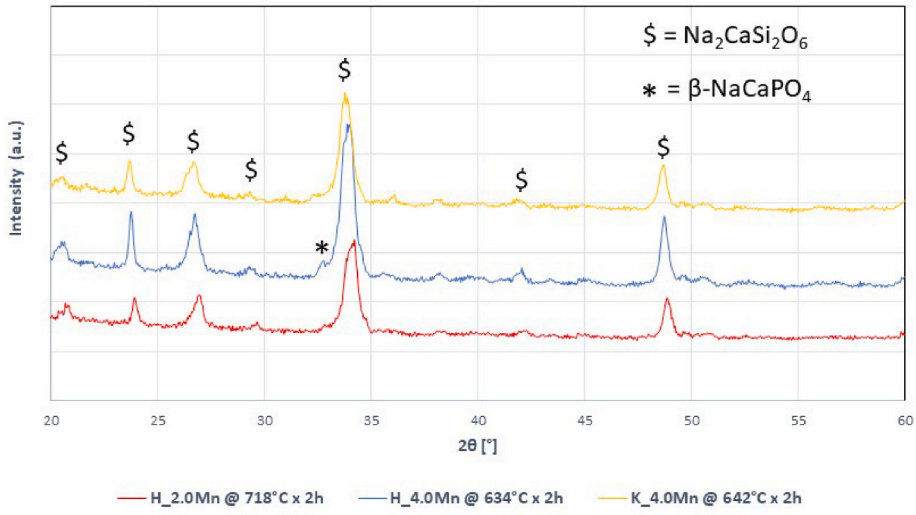

Fig. 5. XRD powder patterns of H 2.0Mn, H 4.0Mn and K 4.0Mn samples after 2 h of thermal treatment at T_c crystallization temperature.

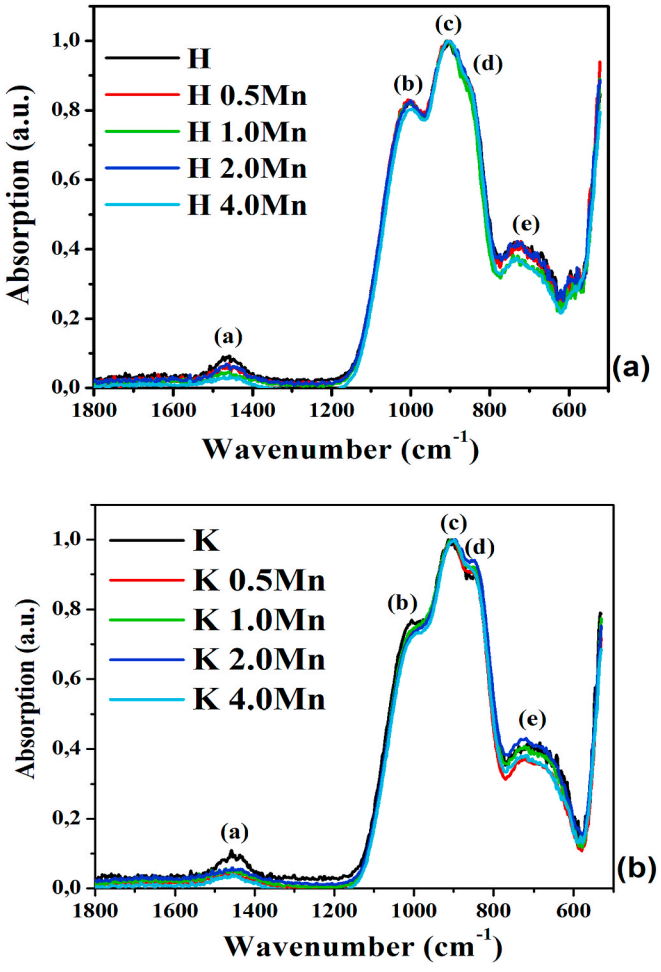

Fig. 6. Normalized ATR FT-IR absorption spectra of (a) H *x*Mn and (b) K *x*Mn glass series. The assignment of bands labelled (a), (b), (c), (d) and (e) to vibration modes is shown in Supplementary Table S1.

processing more difficult for the latter [74].

Fig. 6 shows the normalized ATR FT-IR spectra of the glasses (Fig. 6a and b). The weak band at 1450 cm^{-1} (CO_3^{2-} asymmetric stretching, Table S1) is caused by a surface aging process that leads to carbonatation [75]. The band positioned at 850 cm^{-1}, associated with Si–O–2NBOs, has a higher intensity in the K *x*Mn series compared to the H xMn series, as a consequence of the latter having a higher BOs/NBOs ratio (Table 2) due to the higher content of network modifiers. This was explained by the presence of phosphate in the 45S5 type compositions, because, despite these glasses having a higher molar quantity of modifier ions compared to the SiO_2 content than the P_2O_5 free composition, some of these are associated to the phosphate phase, leading to a lower number of SiO_4 tetrahedra with two NBOs. In the H *x*Mn series the BO/NBO ratio is larger than in the K *x*Mn series (Table 2), which is reflected in the calculated network connectivity [76] value of glass H, this being 2.12 [77] respect to a value of 2.00 for the phosphate free glass (K).

The structural role of Mn in the H *x*Mn and K *x*Mn glass series was qualitatively studied by calculating the ratio between the absorption intensity of the Si–O–Si band and the NBO bands (Si-O-NBO and Si–O–2NBO bands) and analysing changes with the amount of MnO (Fig. 6). For further discussion, both ratios $Abs_{Si\text{-}O\text{-}Si}/Abs_{Si\text{-}O\text{-}NBO}$ and $Abs_{Si\text{-}O\text{-}Si}/Abs_{Si\text{-}O\text{-}2NBO}$ will be labelled as "$Abs_{BO/NBO}$ ratio" since a similar trend was observed (Table 2).

It is well known that Ca^{2+} acts as a modifier ion in the glass structure. Assuming that both Mn^{2+} and Mn^{3+} act as modifier ions by replacing Ca^{2+}, the BO/NBO molar ratio would not be expected to change in the presence of Mn^{2+}, as both metal ions have the same charge leading to the formation of two NBOs for charge-balancing. On the other hand, molar substitution of Ca^{2+} with Mn^{3+} could be expected to increase the number of NBOs needed to charge balance, and the BO/NBO ratio would then be expected to decrease. According to the results presented in Table 2, the $Abs_{BO/NBO}$ ratio slightly decreased within the K *x*Mn series with increasing Mn content. This trend can be explained by the presence of small amounts of Mn^{3+} ions, as detected by H_2-TPR analysis, acting as modifiers. On the other hand, the $Abs_{BO/NBO}$ ratio did not vary significantly with Mn content in the H *x*Mn series. A noticeable decrease of the $Abs_{BO/NBO}$ ratio is detected only for H 4.0Mn glass compared to Mn-free glass, which could be explained with the effect previously described for the K *x*Mn series.

The influence of Mn in both glass series with respect to *in vitro* apatite formation was tested after immersion in Tris buffer or SBF solution, in combination with pH measurement and ionic concentration with immersion time.

Fig. 7a–e show the ATR FT-IR spectra of the H *x*Mn glasses before and after immersion in Tris buffer solution. The release of modifier ions (Na^+ and Ca^{2+}) and the formation of an amorphous silica gel layer on the glass surface are related to the bands positioned between 1140 and 1270 and 800 cm^{-1}, which are associated to Si–O–Si stretching and Si–O–Si

Table 2
Normalized FTIR absorbance attributed to Si–O–Si, Si-O-NBO and Si–O–2NBO bands and their ratio relative of spectra reported in Fig. 5.

Glass	$Abs_{Si\text{-}O\text{-}Si}$	$Abs_{Si\text{-}O\text{-}NBO}$	$Abs_{Si\text{-}O\text{-}2NBO}$	$Abs_{Si\text{-}O\text{-}Si}/Abs_{Si\text{-}O\text{-}NBO}$	$Abs_{Si\text{-}O\text{-}Si}/Abs_{Si\text{-}O\text{-}2NBO}$
H	0.82	0.99	0.89	0.83	0.92
H 0.5Mn	0.82	0.99	0.88	0.83	0.94
H 1.0Mn	0.82	0.99	0.86	0.83	0.95
H 2.0Mn	0.83	1.00	0.89	0.83	0.93
H 4.0Mn	0.80	1.00	0.89	0.80	0.90
K	0.76	1.00	0.89	0.76	0.85
K 0.5Mn	0.74	1.00	0.91	0.74	0.82
K 1.0Mn	0.75	1.00	0.92	0.75	0.81
K 2.0Mn	0.74	1.00	0.94	0.74	0.78
K 4.0Mn	0.73	1.00	0.92	0.73	0.79

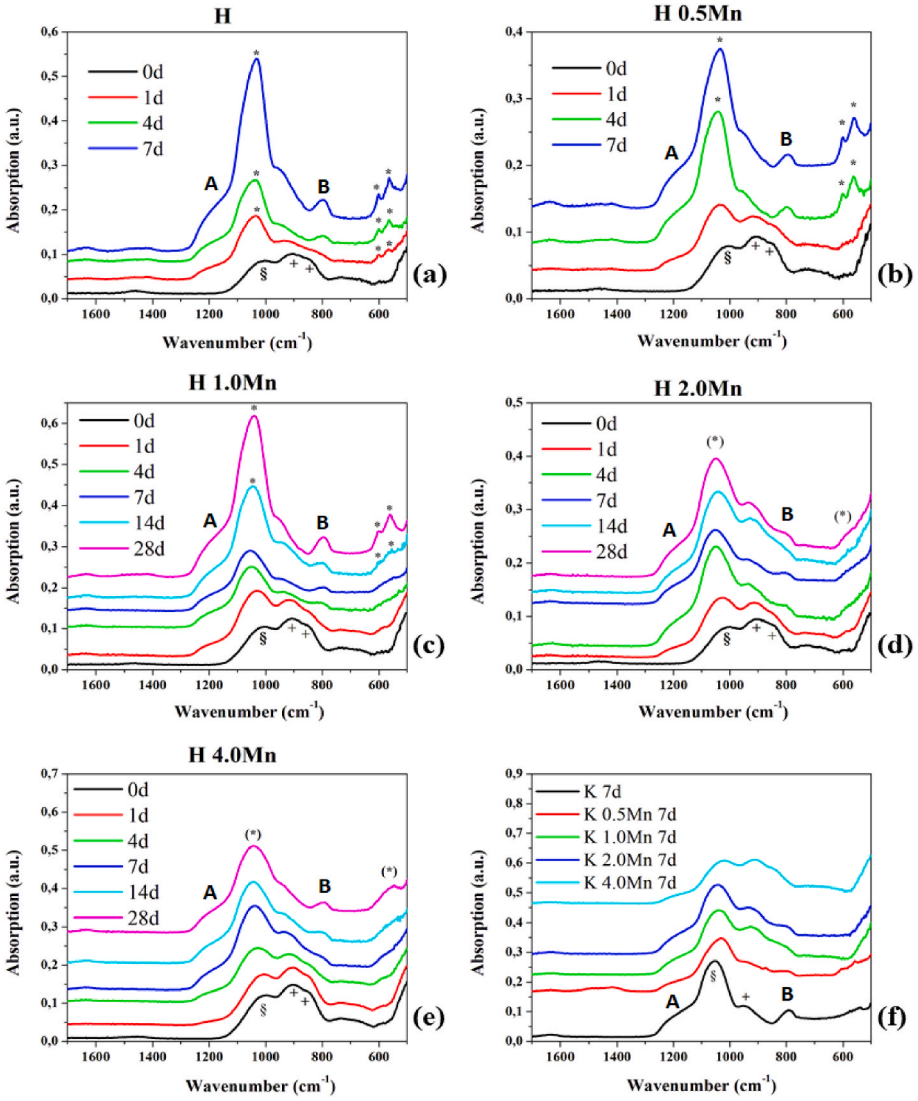

Fig. 7. (a–e) ATR FT-IR absorption spectra of H *x*Mn glass series before and after immersion in Tris buffer solution. (f) ATR FT-IR absorption spectra of K *x*Mn glass series after 7 d of immersion in Tris buffer solution. The assignment of bands labelled A, B, §, +, (*) and * to vibration modes is shown in Supplementary Table S2 [75, 94,95].

bending modes, respectively. The ion release occurrence is then confirmed by an increase in the intensity of the BO band with a simultaneous decrease of the NBO band (Table S2). These changes can be observed for the H series with Mn content up to 2.0 mol% after 1 d of immersion, while this change was observed later (4 d) for the H 4.0Mn glass. The formation of the apatite layer is considered as an indication of *in vitro* bioactivity, which was confirmed with the split band at 560–565 and 600-605 cm^{-1} together with a sharp band positioned between 1035 and 1050 cm^{-1} (Table S2). Apatite formation was detected for glass H (45S5) after 1 d of immersion, while 0.5 and 1.0 mol% Mn contents increased the onset to 4 and 14 d respectively. For samples with higher MnO content (2.0 and 4.0 mol% MnO), the formation of the amorphous calcium phosphate layer was detected only after 28 d.

Fig. 7f shows the ATR FT-IR spectra of the K *x*Mn glasses after

immersion in Tris buffer solution for 7 d. Here, apatite formation is not feasible, as neither the glass nor the immersion medium contains phosphate. The spectra only show the characteristic bands related to cation (Na^+ and Ca^{2+}) release and the formation of an amorphous silica gel layer on the surface. For the glass with the maximum Mn content (K 4.0Mn), these two steps appeared to be delayed.

Fig. 8 shows the relative ion concentrations in Tris buffer solution after immersion for up to 28 d. The concentration of Si, Na, Ca, P and Mn ions in the Tris buffer solution before glass immersion was lower than the limit of quantification of the ICP-OES instrument, meaning that this solution did not contribute to the ion concentration measured at later time points. For this reason, no normalization with respect to initial values detected in the blank samples was necessary. Na concentration was considered to indicate the glass degradability in solution since other ions like Si, Ca and P are involved in the silica gel formation and apatite precipitation.

Similarly, such ion release was clearly seen by ICP analysis (Fig. 8) with a variation of relative Na % in solution varying from 80% to approximately 55% with increasing Mn content. This suggests that the incorporation of Mn increases the glass durability, probably caused by the replacement of Ca^{2+}-O bonds with stronger Mn^{2+}-O or Mn^{3+}-O bonds. Na^+ and Ca^{2+} release in Tris buffer solution was lower for H *x*Mn series when compared with K *x*Mn after 7 d of immersion. This is probably due to the lower NC (or lower BO/NBO ratio, Table 2) of the K *x*Mn glasses in comparison with H *x*Mn glasses [71] According to this, Mn release was higher for the K *x*Mn series with respect to H *x*Mn series, with a maximum of nearly 20 and 10% MnO relative ion concentration, respectively.

Fig. 8 shows the ATR FT-IR spectra and XRD patterns of H *x*Mn and K *x*Mn glasses at different immersion times in SBF solution. Results suggested that the incorporation of Mn into the glasses lowered their ability to induce apatite precipitation [35]. Individual peaks in the XRD pattern were not detected, which is typical for bioactive glasses owing to the high degree of substitution in the apatite lattice and to the nanometre-size of the crystals [78]. The shape of the XRD patterns of samples with low or no Mn content in the H *x*Mn series are typical for apatite formation on bioactive glass surfaces. This agrees with the appearance of the characteristic split band in ATR FT-IR for these compositions. Combined results showed that H *x*Mn glasses with MnO up to 1 mol% induced apatite formation within 7 d. Conversely, glasses with higher MnO content, such as H 2.0Mn glass, induced apatite formation within 28 d, and H 4.0Mn glass did not form apatite within the duration of the experiment. Regarding the K *x*Mn series, K and K 0.5Mn glasses formed apatite within 7 d. Apatite formation was observed on K 1.0Mn glass surface within 14 d, while higher MnO content appeared to inhibit its formation within the duration of the experiment. Fig. 9 shows that the apatite formation, denoted by the presence of the CaP associated stretching band, is faster for the H *x*Mn glass series, suggesting the fundamental role of phosphate in the glass for the precipitation of this phase. The ATR FT-IR bands attributed to carbonate (CO_3^{2-}) incorporation into apatite (1500-1400 and 870 cm^{-1}) were not intense. Therefore, it was not possible to neither confirm nor exclude the formation of carbonated apatite. However, calcite ($CaCO_3$) formation [69] was detected by XRD on the K glass series with up to 2.0 MnO mol%, which could explain the formation of carbonated apatite or calcite precipitation.

Table 3 shows the CMA results with the molar H_2O_2 concentration before and after immersion at various time points. During CMA experiments, gas formation at the glass powder surface was observed, which was most likely related to O_2 decomposition from H_2O_2. The data reported in Table 3 highlight that increasing Mn content in the glass has a beneficial effect on the H_2O_2 decomposition rate. These results showed that there is a positive correlation between the Mn and the CMA of both H *x*Mn and K *x*Mn glass series, conferring them an increase of antioxidant activity properties.

At earlier time points (1 and 4 d) significant differences between the H_2O_2 decomposition activities were observed between the glass series. For example, there was a H_2O_2 concentration difference of slightly over 30% after 1 d between the best performing glass in the H series (H 4.0 Mn) and the composition with the highest H_2O_2 concentration from the K series (K_0.5 Mn). Interestingly, K *x*Mn glass series showed total H_2O_2 decomposition after 4 d of immersion, while a comparable result was only obtained after 7 d for the H *x*Mn glasses.

The glass melted in a reduced atmosphere (H 0.5Mn_red) seemed to

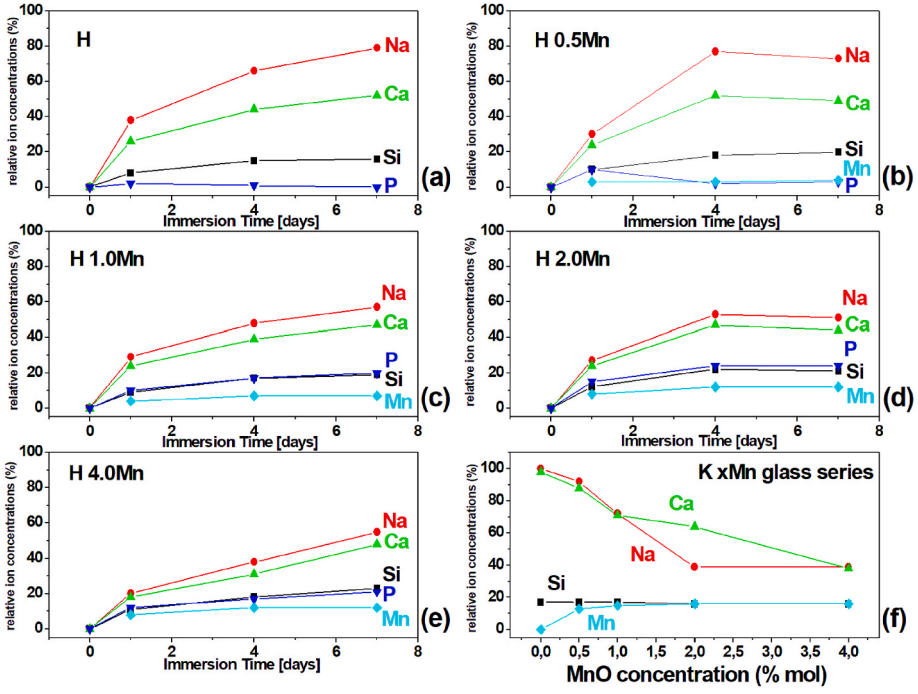

Fig. 8. Relative concentrations (percentage of the ions present in the untreated glass; in %) present in Tris buffer solution for the H (a), H 0.5Mn (b), H 1.0Mn (c), H 2.0Mn (d) and H 4.0Mn (e) glasses after 1, 4, or 7 d of immersion and for the K *x*Mn glass series (f) after 7 d of immersion.

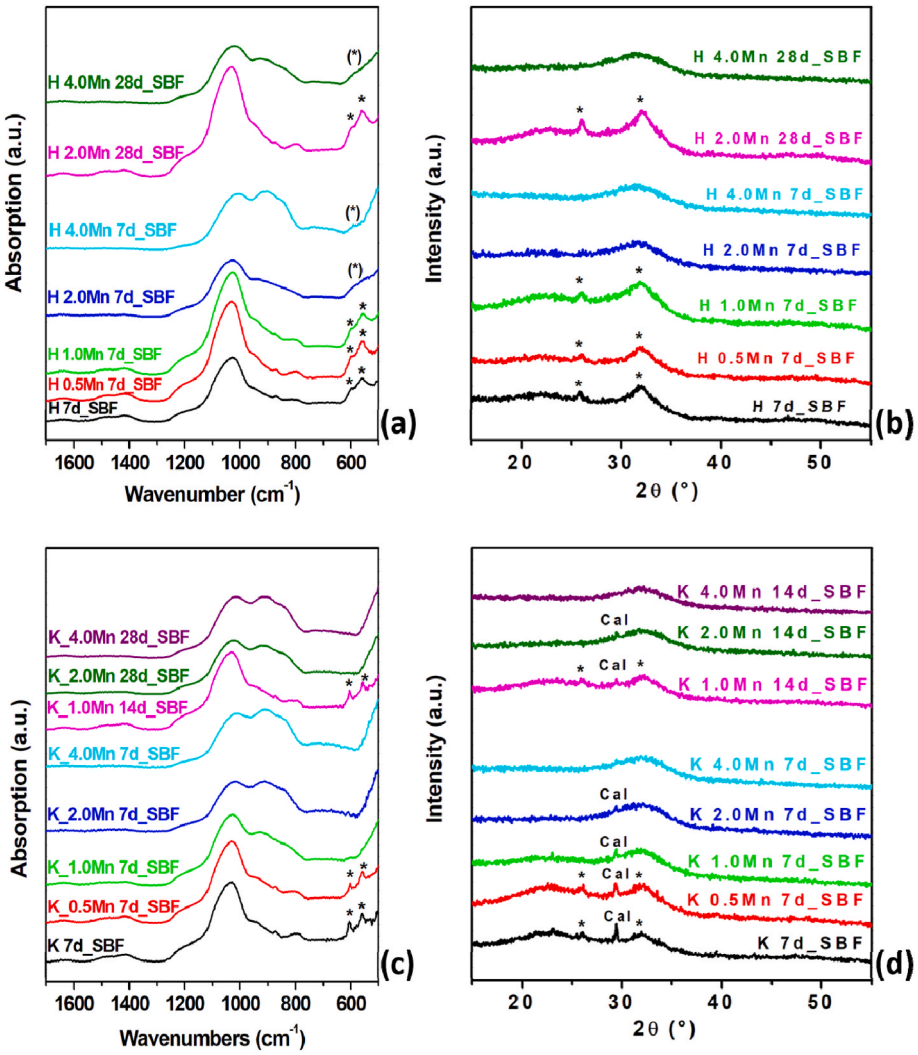

Fig. 9. ATR FT-IR absorption spectra (left, section (a) and (c)) and XRD patterns (right, section (b) and (d)) of glasses in the H *x*Mn and K *x*Mn series at different times of immersion in SBF. Band and reflection labels: * HA/HCA, (*) amorphous CaP layer and Cal Calcite ($CaCO_3$). Curves were stacked to facilitate observing the features without overlapping.

Table 3
Molar H_2O_2 concentration (mol/L) and ratios between the UV–Vis absorption intensity of the Mn^{3+} (500 nm) and Mn^{2+} bands (406 nm) ($AbsMn^{3+}/AbsMn^{2+}$) before (0 d) and after (at 1, 4 or 7 d) immersion in 1.00 mol/L H_2O_2 solution (± standard deviation, n = 3).

	0d		1d		4d		7d	
	H_2O_2 conc. [mol/L]	$AbsMn^{3+}/AbsMn^{2+}$	H_2O_2 conc. [mol/L]	$AbsMn^{3+}/AbsMn^{2+}$	H_2O_2 conc. [mol/L]	$AbsMn^{3+}/AbsMn^{2+}$	H_2O_2 conc. [mol/L]	$AbsMn^{3+}/AbsMn^{2+}$
Blank (H_2O_2)	1.00 ± 0.00	–	1.00 ± 0.00	–	1.00 ± 0.00	–	0.99 ± 0.01	–
H	1.00 ± 0.00	0.96	0.97 ± 0.02	1.06	0.87 ± 0.00	1.07	0.86 ± 0.02	1.07
H 0.5Mn	1.00 ± 0.00	1.81	0.81 ± 0.01	1.78	0.15 ± 0.01	1.51	0.07 ± 0.00	1.55
H 0.5Mn_red	1.00 ± 0.00	0.79	0.74 ± 0.02	0.88	0.23 ± 0.02	0.90	0.09 ± 0.00	0.90
H 1.0Mn	1.00 ± 0.00	2.26	0.69 ± 0.01	1.98	0.09 ± 0.02	1.59	0.02 ± 0.00	1.65
H 2.0Mn	1.00 ± 0.00	2.69	0.70 ± 0.01	2.28	0.07 ± 0.00	1.77	0.02 ± 0.00	1.75
H 4.0Mn	1.00 ± 0.00	2.70	0.64 ± 0.01	2.37	0.08 ± 0.00	1.98	0.02 ± 0.01	1.85
K	1.00 ± 0.00	1.06	0.97 ± 0.02	1.07	0.95 ± 0.02	1.06	0.90 ± 0.04	1.07
K 0.5Mn	1.00 ± 0.00	2.27	0.42 ± 0.01	1.87	0.03 ± 0.00	1.83	0.00 ± 0.00	1.73
K 1.0Mn	1.00 ± 0.00	2.77	0.20 ± 0.01	2.20	0.00 ± 0.00	2.10	0.00 ± 0.00	1.98
K 2.0Mn	1.00 ± 0.00	2.99	0.08 ± 0.00	2.44	0.00 ± 0.00	2.28	0.00 ± 0.00	2.30
K 4.0Mn	1.00 ± 0.00	2.72	0.11 ± 0.00	2.38	0.00 ± 0.00	2.18	0.00 ± 0.00	2.12

catalyse H_2O_2 decomposition better than their air-melt counterpart for early time points (1 d); however, this trend changed at the fourth day of the measurement. Moreover, when comparing the base glasses, no significant CMA was observed up to day 7, which further confirms that for these glass systems there is an association between Mn and an early-stage antioxidant effect. Therefore, it is possible that such approach

would be useful for the tissue regenerative process occurring after a biomaterial is implanted.

pH changes during CMA experiments were measured since it is known that an alkaline pH also enhances the H_2O_2 decomposition rate [79] (Supplementary Table S3). pH increased from 4.20 (1.00 mol/L H_2O_2) to 8–9 after 1 d, stabilizing to 8.5–9 after 4 d. In bioactive type glasses, the pH increase is caused by ion exchange (Na^+) from the glass for protons in solution. Moreover, pH change is also caused by H_2O_2 decomposition since it is a weak acid in solution. However, the effect of pH increase on the H_2O_2 decomposition rate seems negligible at least up to pH 9, as glass K reaches this value at 7 d after immersion while the H_2O_2 concentration is comparably high (0.90 mol/L). Supplementary Figs. S2 and S3 and **S4** show the UV–Vis absorption spectra of all glasses before and after CMA tests. The Mn^{3+} band (at 500 nm) and Mn^{2+} band (at 406 nm) intensity ratios were calculated (Table 3) to quantitatively extract information concerning the Mn ion role in H_2O_2 decomposition. This ratio was solely considered as a qualitative parameter that could aid to identify a trend in Mn^{3+}/Mn^{2+} molar ratio changes. The $AbsMn^{3+}/AbsMn^{2+}$ ratios of the glasses without Mn (H glass and K glass) do not significantly change over time. Nonetheless, for Mn containing glasses (Table 3), this value decreased over time, reaching a stable value when H_2O_2 was completely decomposed at 4 d (K *x*Mn) and 7 d (H *x*Mn glass). Conversely, for glasses melted under a reducing atmosphere, this ratio did not significantly change with immersion time.

I.R. % obtained with the "homogeneous" protocol were negligible, meaning that in these conditions there was no evidence of SOD mimetic activity for any of the glasses (see Table 4). In contrast, I.R. % values obtained with the "heterogeneous" protocol showed significant differences between samples ($p < 0.05$). Substitution of Mn by Ca produced an increase of SOD mimetic activity ranging between approximately 25% (K 4.0Mn) and 40% (H 1.0Mn). No significant difference in SOD mimetic activity was detected between Mn content ranging between 0.5 and 2.0 mol% for the H *x*Mn series. However, a significant decrease of at least 8% occurred between this group and the highest Mn content sample (H 4.0 Mn). A similar trend was observed for the K *x*Mn series, where significant differences were only observed between K - K 4.0Mn and the group corresponding to Mn content between 0.5 and 2.0 Mn.

4. Discussion

When incorporated into silicate glass systems, Mn exists either as Mn^{3+} or Mn^{2+} since higher oxidation states such as 4+ and 7+ are possible but very unlikely [66]. In the studied glass systems, Mn appears to be incorporated as Mn^{2+} and Mn^{3+}, as shown by UV–Vis spectra (Fig. 1). Owing to the significantly larger extinction coefficient of Mn^{3+} (25–100 L cm^{-1} mol^{-1}) compared to Mn^{2+} (0.2–0.5 L cm^{-1} mol^{-1}) [80], the Mn^{3+} band at 500 nm is approximately one-hundred times more intense when compared to that attributed to Mn^{2+} (at 406 nm) if equimolar quantities of the two oxidation states are present. The presence of Mn^{2+} is confirmed by the slight changes in the BO/NBO ratio measured by ATR FT-IR (Fig. 6) and H_2-TPR (Fig. 2), suggesting that only a small Mn fraction is present as Mn^{3+}, and that most of Mn is present as Mn^{2+}, which structural role is very similar to that of Ca^{2+}. If the MnO content in the glass structure is low (0.5 mol %) and the melting is performed in a reducing atmosphere (N_2/H_2 90:10), it is possible to avoid its oxidation and obtain a glass with only Mn^{+2} ions.

Replacing Ca^{2+} with Mn^{2+}/Mn^{3+} ions decreases the possibility of the glass surface to be carbonated, and this result follows the logical progression of phase stability in oxygenated aqueous systems predicted from Eh—pH diagrams for the Mn system [81], where Mn carbonate is unstable compared to hausmannite (Mn_3O_4) and manganite (MnO(OH)) [82].

The substitution of Ca^{2+} with Mn^{2+} in both glass systems leads to the introduction of stronger oxygen bonds, which increase the network compactness. This was confirmed by the higher durability in Tris buffer solution (Table 2) with increasing Mn content. On the other hand, the presence of a small quantity of Mn^{3+} that replaced Ca^{2+} slightly decreases the network connectivity. This was confirmed by a lowering in the glass transition temperature (T_g, Fig. 4) and the slight decrease of the BO/NBO molar ratio shown by FT-IR measurements (Fig. 6) with increasing Mn content. The T_g trend was opposite to the one detected by Gaddam et al. [83], where the introduction of Mn increased T_g. The Authors concluded that Mn ions were mainly present as Mn^{3+}interstitial ions located in the glass network, thus avoiding the silicate network depolymerization. This would therefore suggest that Mn ions (Mn^{2+} and Mn^{3+}) entered the network as modifier ions in our glass system [84].

The role of Mn ions also affected the degradation behaviour. Replacing Ca by Mn in the glass leads to a decrease of Ca^{2+} ions available at the surface, and as both Mn^{2+} and Mn^{3+} ions form stronger bonds with oxygen compared to Ca^{2+} ions, the tendency to react with water decreases. It has also been described by a computational approach that Mn increases the chemical durability of the glass due to its affinity to orthophosphate units, leading to insoluble metal-phosphate segregated areas [85]. Similarly, this was experimentally observed by FTIR: as Mn content increased, the P–O band intensity decreased, correlated to Mn charge balancing the phosphate groups. It would be also possible that Mn^{+3}, when it is present, could readily balance the phosphate unit, leaving Ca and Na ions to depolimerise the silicate network.

The obtained results agree with a lower rate of Ca^{2+} release into Tris buffer solution (52% *vs* 44% of Ca for H and H 4.0Mn, respectively, as well as 98% *vs* 38% of Ca for K and K 4.0Mn, respectively, Fig. 8). The substitution of Mn delayed the apatite inducing ability of the glasses, as formation of an amorphous calcium phosphate and apatite requires the release of Ca^{2+} ions. In Tris buffer and SBF solutions, glasses with 0.5 mol% of MnO formed apatite within 7 d, which was comparable to the base glasses (H and K), while for higher MnO contents apatite formation was delayed. This result agrees with those by Miola et al. [34] that showed how Mn incorporation slightly delayed bioactivity in SBF. These results are also in agreement with those by Srivastava et al., [35] where a content of MnO_2 higher than 1% resulted in a decrease of HCA formation, while the bioactivity was maintained for lower substitutions. However, the substitution in the study was carried out in wt% instead of mol%, which has been reported to have an important effect in structural changes of the glass [50].

The onset of apatite formation also differs between the two series, with glasses in the H *x*Mn series forming apatite slightly faster (7 d) than glasses in the K *x*Mn (14 d) one. Similar trends were observed in a previous study [24,86] where H and K bioactive glasses were modified by the incorporation of CeO_2. The substitution of cerium ions (Ce^{3+} and Ce^{4+}) caused a delay in apatite formation, but this was attributed to cerium ions forming a very low soluble $CePO_4$ phase, which inhibits apatite formation for glasses with more than 3.6 mol% CeO_2.

Relative calcium concentrations in Tris buffer solution were lower for the H *x*Mn series than for the K *x*Mn series. This may be explained

Table 4
Inhibition rate (I.R. %) values with relative standard deviations for the H *x*Mn and K *x*Mn glass series and glasses H 0.5Mn_red. I.R.% is an index of the SOD mimetic activity of a glass following a homogeneous and heterogeneous protocol.

Glass	"homogeneous"	"heterogeneous"
H	−2.3 ± 2.4	52.7 ± 4.1
H 0.5Mn	−0.8 ± 3.5	90.7 ± 0.4
H 0.5Mn_red	−4.3 ± 4.4	91.2 ± 0.8
H 1.0Mn	−1.3 ± 4.9	92.7 ± 0.9
H 2.0Mn	−2.0 ± 1.8	90.7 ± 1.6
H 4.0Mn	−0.4 ± 4.7	81.1 ± 0.1
K	3.6 ± 2.3	41.2 ± 2.9
K 0.5Mn	−2.3 ± 2.7	88.5 ± 0.3
K 1.0Mn	1.2 ± 3.8	89.2 ± 0.1
K 2.0Mn	0.5 ± 1.6	83.8 ± 1.5
K 4.0Mn	2.6 ± 2.2	68.6 ± 5.2

with the interaction between orthophosphate (PO_4^{3-}) and calcium ions in glasses of the H *x*Mn series, possibly delaying calcium release compared to phosphate-free glasses in the K *x*Mn series. In sol-gel glasses a similar effect has been related to non-homogeneous Ca ions distribution in phosphate-containing compositions [87,88]. These studies showed that although the glasses were amorphous, a certain level of intermediate distance order was detected, which greatly influenced the *in vitro* and *in vivo* reactivities. In the ternary Si–Ca–P sol-gel glasses, the Ca^{2+} ions were mainly out of the silicate network and bonded to phosphate. However, these structural considerations differ for melt-derived phospho-silicate glasses and the lower calcium concentrations for H *x*Mn compared to K *x*Mn glasses may be related to the higher NC of the H *x*Mn glasses, slowing down interaction with water [89]. The main factor is here probably apatite precipitation. Ion concentrations in solution are not only affected by ion release from the glass, which increases ion concentrations, but also by precipitation of low solubility phases such as apatite, which decreases the concentrations of the involved ions. During immersion in simulated physiological solutions, availability of phosphate is typically the limiting factor for apatite precipitation [78,90]. Consequently, in K *x*Mn series, calcium does not precipitate as apatite, increasing its concentration in solution, whereas, in the H *x*Mn series, calcium, phosphate and ions such as hydroxyl or carbonates are consumed during apatite formation.

During immersion of H *x*Mn and K *x*Mn glasses in SBF, K *x*Mn glasses showed formation of calcite while this phase was not detected for H *x*Mn glasses (Fig. 9). From a thermodynamic viewpoint, apatite precipitation is favoured compared to calcite precipitation, because of its lower solubility ($Ksp_{HA} = 1 \bullet 10^{-58}$; $Ksp_{Calcite} = 3.8 \bullet 10^{-9}$) [91,92]. However, calcite precipitation is kinetically faster than HA/HCA deposit formation, due to a more favourable combination of one Ca^{2+} ion with one CO_3^{2-} ion to form calcite ($CaCO_3$) in comparison to five Ca^{2+} ions, three PO_4^{3-} ions and one hydroxyl ion to form hydroxyapatite $Ca_5(PO_4)_3(OH)$. Thus, the fast release of Ca^{2+} ions from K *x*Mn glasses owing to the lower network connectivity compared to H *x*Mn glasses, and the absence of phosphate phase in K *x*Mn glasses, caused the solubility product of calcite to be reached when K *x*Mn glasses were soaked in SBF, and therefore its presence as a precipitate. Additionally, the delay in apatite formation for K *x*Mn glasses (Fig. 9) is related to the absence of phosphate ions in their composition, making the SBF solution the only phosphate source for formation of either apatite or an amorphous calcium phosphate layer.

The enzyme-mimicking activity of the glasses derives from replacing Ca^{2+} with Mn, which can interconvert between two oxidation states (Mn^{2+} and Mn^{3+}). This redox behaviour can catalyse the decomposition of H_2O_2 through both a reduction reaction (production of H_2O) and an oxidation reaction (production of O_2) (Tables 3 and 4). During CMA experiments, the $AbsMn^{3+}/AbsMn^{2+}$ ratio decreased and reached comparable values at 7 d of immersion in H_2O_2 for all H *x*Mn and K *x*Mn glasses. Therefore, a comparable Mn^{3+}/Mn^{2+} molar ratios would be expected. This tendency to reach an optimum molar ratio of the redox couple involved in the decomposition of H_2O_2 was already shown in our previous study on the CMA of Ce-containing silicate and phospho-silicate bioactive glasses [86]. Once the optimum Ce^{4+}/Ce^{3+} molar ratio was reached, the maximum rate of H_2O_2 decomposition was observed. The existence of an optimum Mn^{3+}/Mn^{2+} molar ratio of the redox couple involved in the decomposition of H_2O_2 was supported by the CMA results for glasses melted in a reducing atmosphere, as the H_2O_2 decomposition rate for these systems seemed higher than those of the glasses melted in air. We can therefore conclude that the best Mn^{3+}/Mn^{2+} molar ratio is lower than that obtained during synthesis of H *x*Mn and K *x*Mn glasses in air. H 0.5Mn_red glass, which contains almost exclusively Mn^{2+}, showed a better CMA performance compared to H 0.5Mn glass, and we can thus conclude that the presence of Mn^{2+} is essential for the enzymatic activity. Regarding the SOD mimetic activity, the Mn-containing glasses showed a very high enzymatic-like activity, without significant difference between the H 0.5Mn_red and H 0.5Mn glass systems. We have confirmed that for the SOD activity, presence of Mn ions on the glass surface are of importance (Mn^{2+} and Mn^{3+}, see Table 4), because of the heterogeneous catalytic mechanism that involves these ions in the superoxide radical decomposition.

For the Mn free glasses (H and K), the mechanism of the heterogeneous catalysis of H_2O_2 decomposition is still unclear, but it is known that it occurs through catalysis by surface defects and the formation of radical species, such as the hydroxyl (•OH) or hydroperoxyl radical (•OOH) [93]. For silica-based materials, Si–O• radicals present on the material surface can disrupt H_2O_2 molecules, forming •OH and •OOH radicals. Therefore, the higher the surface area of the material is the higher the rate of H_2O_2 decomposition, for which particle size might also have an important influence in this process. Nonetheless, particle size was reported as an important factor in the oxidative stress process, since smaller particles with increased surface area were described to produce higher quantities of ROS [1].

This pathway is less effective than decomposition of H_2O_2 by interconversion of multivalent cations such as Mn, but it becomes relevant for Mn free glasses at later time points (7 d), when the glass surface area is higher after exchange reactions with the solution, leading to depolymerization of the silica network and formation of silanol (Si–OH) groups. However, surface defects in soda-lime-silicate glasses could react with other species before acting as active sites for H_2O_2 decomposition. Consequently, introduction of Mn in the glass structure improves H_2O_2 decomposition by a different mechanism.

The correlation between the antioxidant activity and the phosphate content is interesting because of the clear differences encountered between the glass series. A similar effect was found for Ce-containing bioactive glasses [86], suggesting that the presence of phosphate inhibits the enzyme-like activity of inorganic materials. A possible explanation could be attributed to an increased stability of Mn ions charge balancing phosphate units, which takes them from the Mn^{2+}/Mn^{3+} redox equilibrium, an essential step for CMA to occur. This effect was also reflected on the Mn relative ion concentration for both series.

5. Conclusions

Manganese as MnO was successfully incorporated into soda lime silicate glasses with (H) and without phosphate (K) by molar substitution of CaO (≤4 mol%). Characterization by ATR FT-IR and UV–Vis spectroscopies suggested that Mn^{2+}/Mn^{3+} ions have a comparable structural role as modifiers in the glass silicate network similarly to Ca^{2+} ions. Manganese was mainly present as Mn^{2+}; however, a fraction of Mn^{2+} ions oxidized to Mn^{3+} ions by melting oxidizing conditions (air). By contrast, Mn oxidation to a +3 state was avoided when melting under a reducing atmosphere (N_2/H_2 90:10) for the 45S5 type glass with 0.5 mol% MnO content. Replacing Ca^{2+} ions with Mn^{2+}/Mn^{3+} ions leads to the introduction of stronger bonds with oxygen, resulting in increased network compactness. This structural change results in the increased stability in Tris buffer solution with increasing Mn content. As a result, the onset of apatite formation was delayed with increasing Mn content during *in vitro* testing. Interestingly, this trend was reversed for the antioxidant activity of the glasses, with their CMA and SOD mimetic activity improved by Mn content. This was associated with the interconversion between Mn^{2+} and Mn^{3+} oxidation states, which can decompose both hydrogen peroxide and superoxide anion through heterogeneous redox reactions. A distinct improvement in this effect was obtained for the phosphate free glass series (K), for which an early-stage oxidative stress effect reduction was observed for glass with more than 1 mol% MnO, showing the important role of P_2O_5 on the ability of Mn to undergo this interconversion. Further studies will then be required to understand the associated structural mechanisms. Consequently, a balance between the optimum phosphate and Mn content is of importance as to maximise the antioxidant potential of the glass while maintaining its bioactivity expressed as the onset of apatite formation. The results

here presented can be then used as a basis to further explore the benefits of incorporating Mn as an antioxidant ion when developing bioactive glasses for bone replacement applications.

Funding

This study was funded by the German Research Foundation (DFG; grant BR 4608/7-1).

Declaration of competing interest

The authors declare that they have no known competing financial interests or personal relationships that could have appeared to influence the work reported in this paper.

Acknowledgements

The authors would like to thank Steffi Ebbinghaus for dilatometry measurements and Steffen Müller for DSC measurements. MA acknowledges Erasmus+ funding, which made his research stay in Germany possible. DSB and ATCJ acknowledge funding by the German Research Foundation (DFG; grant BR 4608/7-1).

Appendix A. Supplementary data

Supplementary data to this article can be found online at https://doi.org/10.1016/j.ceramint.2023.10.091.

References

[1] P.-A. Mouthuy, S.J.B. Snelling, S.G. Dakin, L. Milković, A.Č. Gašparović, A.J. Carr, N. Žarković, Biocompatibility of implantable materials: an oxidative stress viewpoint, Biomaterials 109 (2016) 55–68, https://doi.org/10.1016/j.biomaterials.2016.09.010.

[2] L.L. Hench, R.J. Splinter, W.C. Allen, T.K. Greenlee, Bonding mechanisms at the interface of ceramic prosthetic materials, J. Biomed. Mater. Res. 5 (6) (1971) 117–141, https://doi.org/10.1002/jbm.820050611.

[3] L.L. Hench, The story of Bioglass, J. Mater. Sci. Mater. Med. 17 (11) (2006) 967–978, https://doi.org/10.1007/s10856-006-0432-z.

[4] V. Mourino, J.P. Cattalini, A.R. Boccaccini, Metallic ions as therapeutic agents in tissue engineering scaffolds: an overview of their biological applications and strategies for new developments, J. R. Soc. Interface 9 (68) (2012) 401–419, https://doi.org/10.1098/rsif.2011.0611.

[5] D.S. Brauer, Bioactive glasses-structure and properties, Angew. Chem. Int. Ed. 54 (14) (2015) 4160–4181, https://doi.org/10.1002/anie.201405310.

[6] R. Hill, An alternative view of the degradation of Bioglass, J. Mater. Sci. Lett. 15 (13) (1996) 1122–1125, https://doi.org/10.1007/BF00539955.

[7] R.G. Hill, D.S. Brauer, Predicting the bioactivity of glasses using the network connectivity or split network models, J. Non-Cryst. Solids 357 (24) (2011) 3884–3887, https://doi.org/10.1016/j.jnoncrysol.2011.07.025.

[8] M. Bellantone, H.D. Williams, L.L. Hench, Broad-spectrum bactericidal activity of Ag2O-doped bioactive glass, Antimicrob. Agents Chemother. 46 (6) (2002) 1940–1945, https://doi.org/10.1128/AAC.46.6.1940-1945.2002.

[9] M. Bellantone, N.J. Coleman, L.L. Hench, Bacteriostatic action of a novel four-component bioactive glass, J. Biomed. Mater. Res. 51 (3) (2000) 484–490, https://doi.org/10.1002/1097-4636(20000905)51:3<484::AID-JBM24>3.0.CO;2-4.

[10] M. Yazdimamaghani, D. Vashaee, S. Assefa, K.J. Walker, S.V. Madihally, G. A. Köhler, L. Tayebi, Hybrid macroporous gelatin/bioactive-glass/nanosilver scaffolds with controlled degradation behavior and antimicrobial activity for bone tissue engineering, J. Biomed. Nanotechnol. 10 (6) (2014) 911–931, https://doi.org/10.1166/jbn.2014.1783.

[11] J.J. Blaker, S.N. Nazhat, A.R. Boccaccini, Development and characterisation of silver-doped bioactive glass-coated sutures for tissue engineering and wound healing applications, Biomaterials 25 (7–8) (2004) 1319–1329, https://doi.org/10.1016/j.biomaterials.2003.08.007.

[12] S.P. Valappil, D. Ready, E.A.A. Neel, D.M. Pickup, W. Chrzanowski, L.A. O'Dell, R. J. Newport, M.E. Smith, M. Wilson, J.C. Knowles, Antimicrobial gallium-doped phosphate-based glasses, Adv. Funct. Mater. 18 (5) (2008) 732–741, https://doi.org/10.1002/adfm.200700931.

[13] S.P. Valappil, D. Ready, E.A. Abou Neel, D.M. Pickup, L.A. O'Dell, W. Chrzanowski, J. Pratten, R.J. Newport, M.E. Smith, M. Wilson, J.C. Knowles, Controlled delivery of antimicrobial gallium ions from phosphate-based glasses, Acta Biomater. 5 (4) (2009) 1198–1210, https://doi.org/10.1016/j.actbio.2008.09.019.

[14] E. Dietrich, H. Oudadesse, A. Lucas-Girot, M. Mami, In *vitro* bioactivity of melt-derived glass 46S6 doped with magnesium, J. Biomed. Mater. Res. A 88A (4) (2009) 1087–1096, https://doi.org/10.1002/jbm.a.31901.

[15] P.J. Meunier, C. Roux, E. Seeman, S. Ortolani, J.E. Badurski, T.D. Spector, J. Cannata, A. Balogh, E.-M. Lemmel, S. Pors-Nielsen, R. Rizzoli, H.K. Genant, J.-Y. Reginster, The effects of strontium ranelate on the risk of vertebral fracture in women with postmenopausal osteoporosis, N. Engl. J. Med. 350 (5) (2004) 459–468, https://doi.org/10.1056/NEJMoa022436.

[16] V. Aina, G. Malavasi, A. Fiorio Pla, L. Munaron, C. Morterra, Zinc-containing bioactive glasses: surface reactivity and behaviour towards endothelial cells, Acta Biomater. 5 (4) (2009) 1211–1222, https://doi.org/10.1016/j.actbio.2008.10.020.

[17] L. Courthéoux, J. Lao, J.-M. Nedelec, E. Jallot, Controlled bioactivity in zinc-doped Sol−Gel-derived binary bioactive glasses, J. Phys. Chem. C 112 (35) (2008) 13663–13667, https://doi.org/10.1021/jp8044498.

[18] W. Fan, R. Crawford, Y. Xiao, Enhancing in vivo vascularized bone formation by cobalt chloride-treated bone marrow stromal cells in a tissue engineered periosteum model, Biomaterials 31 (13) (2010) 3580–3589, https://doi.org/10.1016/j.biomaterials.2010.01.083.

[19] D.S. Brauer, N. Karpukhina, M.D. O'Donnell, R.V. Law, R.G. Hill, Fluoride-containing bioactive glasses: effect of glass design and structure on degradation, PH and apatite formation in simulated body Fluid, Acta Biomater. 6 (8) (2010) 3275–3282, https://doi.org/10.1016/j.actbio.2010.01.043.

[20] E. Lynch, D.S. Brauer, N. Karpukhina, D.G. Gillam, R.G. Hill, Multi-component bioactive glasses of varying fluoride content for treating dentin hypersensitivity, Dent. Mater. 28 (2) (2012) 168–178, https://doi.org/10.1016/j.dental.2011.11.021.

[21] J.P. Pessan, N.S. Al-Ibrahim, M.A.R. Buzalaf, K.J. Toumba, Slow-release fluoride devices: a literature review, J. Appl. Oral Sci. 16 (4) (2008) 238–244, https://doi.org/10.1590/S1678-77572008000400003.

[22] P. Christel, A. Meunier, J.-M. Dorlot, J.-M. Crolet, J. Witvoet, L. Sedel, P. Boutin, Biomechanical compatibility and design of ceramic implants for orthopedic surgery, Ann. N. Y. Acad. Sci. 523 (1 Bioceramics) (1988) 234–256, https://doi.org/10.1111/j.1749-6632.1988.tb38516.x.

[23] V. Cannillo, A. Sola, Potassium-based composition for a bioactive glass, Ceram. Int. 35 (8) (2009) 3389–3393, https://doi.org/10.1016/j.ceramint.2009.06.011.

[24] V. Nicolini, E. Gambuzzi, G. Malavasi, L. Menabue, M.C. Menziani, G. Lusvardi, A. Pedone, F. Benedetti, P. Luches, S. D'Addato, S. Valeri, Evidence of catalase mimetic activity in Ce^{3+}/Ce^{4+} doped bioactive glasses, J. Phys. Chem. B 119 (10) (2015) 4009–4019, https://doi.org/10.1021/jp511737b.

[25] S. Jebahi, H. Oudadesse, H. el Feki, T. Rebai, H. Keskes, P. Pellen, A. el Feki, Antioxidative/oxidative effects of strontium-doped bioactive glass as bone graft. In vivo assays in ovariectomised rats, J. Appl. Biomed. 10 (4) (2012) 195–209, https://doi.org/10.2478/v10136-012-0009-8.

[26] C. Wu, W. Fan, Y. Zhu, M. Gelinsky, J. Chang, G. Cuniberti, V. Albrecht, T. Friis, Y. Xiao, Multifunctional magnetic mesoporous bioactive glass scaffolds with a hierarchical pore structure, Acta Biomater. 7 (10) (2011) 3563–3572, https://doi.org/10.1016/j.actbio.2011.06.028.

[27] B.R. Barrioni, E. Norris, S. Li, P. Naruphontjirakul, J.R. Jones, M. de M. Pereira, Osteogenic potential of sol–gel bioactive glasses containing manganese, J. Mater. Sci. Mater. Med. 30 (7) (2019) 86, https://doi.org/10.1007/s10856-019-6288-9.

[28] U. Pantulap, M. Arango-Ospina, A.R. Boccaccini, Bioactive glasses incorporating less-common ions to improve biological and physical properties, J. Mater. Sci. Mater. Med. 33 (1) (2021) 3, https://doi.org/10.1007/s10856-021-06626-3.

[29] J.V. Rau, A. De Stefanis, K. Barbaro, M. Fosca, V.G. Yankova, R. Matassa, S. A. Nottola, Q. Nawaz, M.S. Ali, W. Peukert, A.R. Boccaccini, Adipogenic, chondrogenic, osteogenic, and antimicrobial features of glass ceramic material supplemented with manganese, J. Non-Cryst. Solids 559 (2021), 120709, https://doi.org/10.1016/j.jnoncrysol.2021.120709.

[30] M. Miola, C.V. Brovarone, G. Maina, F. Rossi, L. Bergandi, D. Ghigo, S. Saracino, M. Maggiora, R.A. Canuto, G. Muzio, E. Vernè, In vitro study of manganese-doped bioactive glasses for bone regeneration, Mater. Sci. Eng. C 38 (2014) 107–118, https://doi.org/10.1016/j.msec.2014.01.045.

[31] M. Miola, J. Massera, A. Cochis, A. Kumar, L. Rimondini, E. Vernè, Tellurium: a new active element for innovative multifunctional bioactive glasses, Mater. Sci. Eng. C 123 (2021), 111957, https://doi.org/10.1016/j.msec.2021.111957.

[32] G. El-Damraw, H. Doweidar, H. Kamal, Characterization of new categories of bioactive based tellurite and silicate glasses, Silicon 9 (2017) 503–509, https://doi.org/10.1007/s12633-014-9248-5.

[33] B. Karakuzu-İkizler, P. Terzioğlu, B.S. Oduncu-Tekerek, S. Yücel, Effect of selenium incorporation on the structure and in vitro bioactivity of 45S5 Bioglass, J. Australas. Ceram. Soc. 56 (2) (2020) 697–709, https://doi.org/10.1007/s41779-019-00388-6.

[34] M. Miola, C.V. Brovarone, G. Maina, F. Rossi, L. Bergandi, D. Ghigo, S. Saracino, M. Maggiora, R.A. Canuto, G. Muzio, E. Vernè, In vitro study of manganese-doped bioactive glasses for bone regeneration, Mater. Sci. Eng. C 38 (2014) 107–118, https://doi.org/10.1016/j.msec.2014.01.045.

[35] A.K. Srivastava, R. Pyare, S.P. Singh, *In vitro* bioactivity and physical–mechanical properties of MnO_2 substituted 45S5 bioactive glasses and glass-ceramics, J. Biomater. Tissue Eng. 2 (3) (2012) 249–258, https://doi.org/10.1166/jbt.2012.1043.

[36] B.R. Barrioni, A.C. Oliveira, M. de Fátima Leite, M. de Magalhães Pereira, Sol–gel-derived manganese-releasing bioactive glass as a therapeutic approach for bone tissue engineering, J. Mater. Sci. 52 (15) (2017) 8904–8927, https://doi.org/10.1007/s10853-017-0944-6.

[37] B.R. Barrioni, P. Naruphontjirakul, E. Norris, S. Li, N.L. Kelly, J.V. Hanna, M. M. Stevens, J.R. Jones, M. de M. Pereira, Effects of manganese incorporation on the morphology, structure and cytotoxicity of spherical bioactive glass nanoparticles, J. Colloid Interface Sci. 547 (2019) 382–392, https://doi.org/10.1016/j.jcis.2019.04.016.

[38] Q. Nawaz, M.A.U. Rehman, A. Burkovski, J. Schmidt, A.M. Beltrán, A. Shahid, N. K. Alber, W. Peukert, A.R. Boccaccini, Synthesis and characterization of manganese containing mesoporous bioactive glass nanoparticles for biomedical applications, J. Mater. Sci. Mater. Med. 29 (5) (2018) 64, https://doi.org/10.1007/s10856-018-6070-4.

[39] S. Kapoor, D. Brazete, I.C. Pereira, G. Bhatia, M. Kaur, L.F. Santos, D. Banerjee, A. Goel, J.M.F. Ferreira, Impact of transition metal ions on the structure and bioactivity of alkali-free bioactive glasses, J. Non-Cryst. Solids 506 (2019) 98–108, https://doi.org/10.1016/j.jnoncrysol.2018.12.003.

[40] J.D. Aguirre, V.C. Culotta, Battles with iron: manganese in oxidative stress protection, J. Biol. Chem. 287 (17) (2012) 13541–13548, https://doi.org/10.1074/jbc.R111.312181.

[41] N.A. Law, M.T. Caudle, V.L. Pecoraro, Manganese redox enzymes and model systems: properties, structures, and reactivity, Adv. Inorg. Chem. 46 (1998) 305–440, https://doi.org/10.1016/S0898-8838(08)60152-X. Elsevier.

[42] J.H. Beattie, A. Avenell, Trace element nutrition and bone metabolism, Nutr. Res. Rev. 5 (1) (1992) 167–188, https://doi.org/10.1079/NRR19920013.

[43] F. Lüthen, U. Bulnheim, P.D. Müller, J. Rychly, H. Jesswein, J.G.B. Nebe, Influence of manganese ions on cellular behavior of human osteoblasts in vitro, Biomol. Eng. 24 (5) (2007) 531–536, https://doi.org/10.1016/j.bioeng.2007.08.003.

[44] P.M.C. Torres, S.I. Vieira, A.R. Cerqueira, S. Pina, O.A.B. da Cruz Silva, J.C. C. Abrantes, J.M.F. Ferreira, Effects of Mn-doping on the structure and biological properties of β-tricalcium phosphate, J. Inorg. Biochem. 136 (2014) 57–66, https://doi.org/10.1016/j.jinorgbio.2014.03.013.

[45] W. Fujitani, Y. Hamada, N. Kawaguchi, S. Mori, K. Daito, A. Uchinaka, T. Matsumoto, Y. Kojima, M. Daito, T. Nakano, N. Matsuura, Synthesis of Hydroxyapatite Contining Manganese and its Evaluation of Biocompatibility, 2010, https://doi.org/10.11344/nano.2.37. (Accessed 4 July 2019).

[46] Y.-J. Bae, M.-H. Kim, Manganese supplementation improves mineral density of the spine and femur and serum osteocalcin in rats, Biol. Trace Elem. Res. 124 (1) (2008) 28–34, https://doi.org/10.1007/s12011-008-8119-6.

[47] S. Fujibayashi, A comparative study between in vivo bone ingrowth and in vitro apatite formation on Na2O–CaO–SiO2 glasses, Biomaterials 24 (8) (2003) 1349–1356, https://doi.org/10.1016/S0142-9612(02)00511-2.

[48] G. Malavasi, G. Lusvardi, Composition and morphology effects on catalase mimetic activity of potential bioactive glasses, Ceram. Int. 46 (16) (2020) 25854–25864, https://doi.org/10.1016/j.ceramint.2020.07.067.

[49] P. Pascuta, G. Borodi, N. Jumate, I. Vida-Simiti, D. Viorel, E. Culea, The structural role of manganese ions in some zinc phosphate glasses and glass ceramics, J. Alloys Compd. 504 (2) (2010) 479–483, https://doi.org/10.1016/j.jallcom.2010.05.147.

[50] M.D. O'Donnell, R.G. Hill, Influence of strontium and the importance of glass chemistry and structure when designing bioactive glasses for bone regeneration, Acta Biomater. 6 (7) (2010) 2382–2385, https://doi.org/10.1016/j.actbio.2010.01.006.

[51] N.N. Greenwood, A. Earnshaw, Chemistry of the Elements, second ed., Butterworth-Heinemann, Oxford ; Boston, 1997.

[52] I. Bratu, I. Ardelean, A. Barbu, V. Mih, D. Maniu, G. Botezan, Spectroscopic investigation of some lead phosphate oxide glasses containing manganese ions, J. Mol. Struct. 482–483 (1999) 689–692, https://doi.org/10.1016/S0022-2860(98)00940-5.

[53] D.K. Durga, N. Veeraiah, Role of manganese ions on the stability of ZnF2–P2O5–TeO2 glass system by the study of dielectric dispersion and some other physical properties, J. Phys. Chem. Solid. 64 (1) (2003) 133–146, https://doi.org/10.1016/S0022-3697(02)00273-1.

[54] N.K. Mohan, M.R. Reddy, C.K. Jayasankar, N. Veeraiah, Spectroscopic and dielectric studies on MnO doped PbO–Nb2O5–P2O5 glass system, J. Alloys Compd. 458 (1–2) (2008) 66–76, https://doi.org/10.1016/j.jallcom.2007.04.143.

[55] I. Konidakis, C.-P.E. Varsamis, E.I. Kamitsos, D. Möncke, D. Ehrt, Structure and properties of mixed Strontium−Manganese metaphosphate glasses, J. Phys. Chem. C 114 (19) (2010) 9125–9138, https://doi.org/10.1021/jp101750t.

[56] H.-M. Kim, F. Miyaji, T. Kokubo, C. Ohtsuki, T. Nakamura, Bioactivity of Na2O-CaO-SiO2 glasses, J. Am. Ceram. Soc. 78 (9) (1995) 2405–2411, https://doi.org/10.1111/j.1151-2916.1995.tb08677.x.

[57] N.W. Hurst, S.J. Gentry, A. Jones, B.D. McNicol, Temperature programmed reduction, Catal. Rev. 24 (2) (1982) 233–309, https://doi.org/10.1080/03602458208079654.

[58] F. Kapteijn, L. Singoredjo, A. Andreini, J.A. Moulijn, Activity and selectivity of pure manganese oxides in the selective catalytic reduction of nitric oxide with ammonia, Appl. Catal. B Environ. 3 (2–3) (1994) 173–189, https://doi.org/10.1016/0926-3373(93)E0034-9.

[59] L. Müller, F.A. Müller, Preparation of SBF with different HCO3- content and its influence on the composition of biomimetic apatites, Acta Biomater. 2 (2) (2006) 181–189, https://doi.org/10.1016/j.actbio.2005.11.001.

[60] A.L.B. Maçon, T.B. Kim, E.M. Valliant, K. Goetschius, R.K. Brow, D.E. Day, A. Hoppe, A.R. Boccaccini, I.Y. Kim, C. Ohtsuki, T. Kokubo, A. Osaka, M. Vallet-Regí, D. Arcos, L. Fraile, A.J. Salinas, A.V. Teixeira, Y. Vueva, R.M. Almeida, M. Miola, C. Vitale-Brovarone, E. Verné, W. Höland, J.R. Jones, A unified in vitro evaluation for apatite-forming ability of bioactive glasses and their variants, J. Mater. Sci. Mater. Med. 26 (2) (2015) 115, https://doi.org/10.1007/s10856-015-5403-9.

[61] H. Ukeda, D. Kawana, S. Maeda, M. Sawamura, Spectrophotometric assay for superoxide dismutase based on the reduction of highly water-soluble tetrazolium salts by xanthine-xanthine oxidase, Biosci. Biotechnol. Biochem. 63 (3) (1999) 485–488, https://doi.org/10.1271/bbb.63.485.

[62] Y. Sheng, I.A. Abreu, D.E. Cabelli, M.J. Maroney, A.-F. Miller, M. Teixeira, J. S. Valentine, Superoxide dismutases and superoxide reductases, Chem. Rev. 114 (7) (2014) 3854–3918, https://doi.org/10.1021/cr4005296.

[63] H. Kappler, Crystal field spectra and geochemistry of transition metal ions in silicate melts and glasses, Am. Mineral. 77 (1992) 62–75.

[64] L. Biernacki, S. Pokrzywnicki, The thermal decomposition of manganese carbonate thermogravimetry and exoemission of electrons, J. Therm. Anal. Calorim. 55 (1) (1999) 227–232, https://doi.org/10.1023/A:1010165029080.

[65] A. Terczynska-Madej, K. Cholewa-Kowalska, M. Laczka, The effect of silicate network modifiers on colour and electron spectra of transition metal ions, Opt. Mater. 32 (11) (2010) 1456–1462, https://doi.org/10.1016/j.optmat.2010.05.024.

[66] A.J. Werner, in: C.R. Bamford (Ed.), Colour Generation and Control in Glass, Elsevier Scientific Publishing Co., Amsterdam and New York, 1977, p. 224, https://doi.org/10.1002/col.5080030317. Price, $34.95. Color Res. Appl. 1978, 3 (3), 156–156.

[67] S.M. Lee, K.H. Park, S.S. Kim, D.W. Kwon, S.C. Hong, Effect of the Mn oxidation state and lattice oxygen in Mn-based TiO_2 catalysts on the low-temperature selective catalytic reduction of NO by NH_3, J. Air Waste Manag. Assoc. 62 (9) (2012) 1085–1092, https://doi.org/10.1080/10962247.2012.696532.

[68] X. Niu, H. Wei, K. Tang, W. Liu, G. Zhao, Y. Yang, Solvothermal synthesis of 1D nanostructured Mn_2O_3 : effect of Ni^{2+} and Co^{2+} substitution on the catalytic activity of nanowires, RSC Adv. 5 (81) (2015) 66271–66277, https://doi.org/10.1039/C5RA14618F.

[69] PCPFWIN, JCPDS International Center for Diffraction Data, Swarthmore, PA, USA, 2002.

[70] K. Hurrell-Gillingham, I.M. Reaney, C.A. Miller, A. Crawford, P.V. Hatton, Devitrification of ionomer glass and its effect on the in vitro biocompatibility of glass-ionomer cements, Biomaterials 24 (18) (2003) 3153–3160, https://doi.org/10.1016/S0142-9612(03)00124-8.

[71] M. Plewinski, K. Schickle, M. Lindner, A. Kirsten, M. Weber, H. Fischer, The effect of crystallization of bioactive Bioglass 45S5 on apatite formation and degradation, Dent. Mater. 29 (12) (2013) 1256–1264, https://doi.org/10.1016/j.dental.2013.09.016.

[72] M.B. Volf, *Chemical Approach to Glass*; Glass Science and Technology, Elsevier, Amsterdam ; New York, 1984.

[73] A. Tilocca, A.N. Cormack, Structural effects of phosphorus inclusion in bioactive silicate glasses, J. Phys. Chem. B 111 (51) (2007) 14256–14264, https://doi.org/10.1021/jp075677o.

[74] J.R. Jones, Review of bioactive glass: from hench to hybrids, Acta Biomater. 9 (1) (2013) 4457–4486, https://doi.org/10.1016/j.actbio.2012.08.023.

[75] M. Cerruti, C. Morterra, Carbonate Formation on bioactive glasses, Langmuir 20 (15) (2004) 6382–6388, https://doi.org/10.1021/la049723c.

[76] J.E. Shelby, Introduction to Glass Science and Technology, second ed., Royal Society of Chemistry, Cambridge, 2005.

[77] D. Sriranganathan, N. Kanwal, K.A. Hing, R.G. Hill, Strontium substituted bioactive glasses for tissue engineered scaffolds: the importance of octacalcium phosphate, J. Mater. Sci. Mater. Med. 27 (2) (2016) 39, https://doi.org/10.1007/s10856-015-5653-6.

[78] M.D. O'Donnell, S.J. Watts, R.G. Hill, R.V. Law, The effect of phosphate content on the bioactivity of soda-lime-phosphosilicate glasses, J. Mater. Sci. Mater. Med. 20 (8) (2009) 1611–1618, https://doi.org/10.1007/s10856-009-3732-2.

[79] W.D. Nicoll, A.F. Smith, Stability of dilute alkaline solutions of hydrogen peroxide, Ind. Eng. Chem. 47 (12) (1955) 2548–2554, https://doi.org/10.1021/ie50552a051.

[80] D. Möncke, M. Papageorgiou, A. Winterstein-Beckmann, N. Zacharias, Roman glasses coloured by dissolved transition metal ions: redox-reactions, optical spectroscopy and ligand field theory, J. Archaeol. Sci. 46 (2014) 23–36, https://doi.org/10.1016/j.jas.2014.03.007.

[81] M. Pourbaix, Atlas of Electrochemical Equilibria in Aqueous Solutions Retrieved, Electronic Books database, 1974.

[82] J.L. Hager, Sorption of manganese and silica by clay and carbonate, Mar. Chem. 9 (3) (1980) 199–209, https://doi.org/10.1016/0304-4203(80)90039-0.

[83] A. Gaddam, H.R. Fernandes, D.U. Tulyaganov, M.J. Pascual, J.M.F. Ferreira, Role of manganese on the structure, crystallization and sintering of non-stoichiometric lithium disilicate glasses, RSC Adv. 4 (26) (2014), 13581, https://doi.org/10.1039/c3ra46393a.

[84] A.K. Varshneya, Chemical strengthening of glass: lessons learned and yet to Be learned: chemical strengthening of glass, Int. J. Appl. Glass Sci. 1 (2) (2010) 131–142, https://doi.org/10.1111/j.2041-1294.2010.00010.x.

[85] G. Malavasi, A. Pedone, The effect of the incorporation of catalase mimetic activity cations on the structural, thermal and chemical durability properties of the 45S5 Bioglass, Acta Mater. 229 (2022), 117801, https://doi.org/10.1016/j.actamat.2022.117801.

[86] V. Nicolini, G. Malavasi, L. Menabue, G. Lusvardi, F. Benedetti, S. Valeri, P. Luches, Cerium-doped bioactive 45S5 glasses: spectroscopic, redox, bioactivity and biocatalytic properties, J. Mater. Sci. 52 (15) (2017) 8845–8857, https://doi.org/10.1007/s10853-017-0867-2.

[87] M. Vallet-Regi, A. Salinas, Role of the short distance order in glass reactivity, Materials 11 (3) (2018) 415, https://doi.org/10.3390/ma11030415.

[88] M. Vallet-Regí, A.J. Salinas, J. Ramírez-Castellanos, J.M. González-Calbet, Nanostructure of bioactive Sol−Gel glasses and Organic−Inorganic hybrids, Chem. Mater. 17 (7) (2005) 1874–1879, https://doi.org/10.1021/cm047956j.

[89] A. Tilocca, A.N. Cormack, Surface signatures of bioactivity: MD simulations of 45S and 65S silicate glasses, Langmuir 26 (1) (2010) 545–551, https://doi.org/10.1021/la902548f.

[90] M. Mneimne, R.G. Hill, A.J. Bushby, D.S. Brauer, High phosphate content significantly increases apatite formation of fluoride-containing bioactive glasses, Acta Biomater. 7 (4) (2011) 1827–1834, https://doi.org/10.1016/j.actbio.2010.11.037.

[91] Y. Zhu, B. Huang, Z. Zhu, H. Liu, Y. Huang, X. Zhao, M. Liang, Characterization, dissolution and solubility of the hydroxypyromorphite–hydroxyapatite solid solution [(PbxCa1−x)5(PO4)3OH] at 25 °C and PH 2–9, Geochem. Trans. 17 (1) (2016) 2, https://doi.org/10.1186/s12932-016-0034-8.

[92] J.W. Morse, A. Mucci, F.J. Millero, The solubility of calcite and aragonite in seawater of 35%. Salinity at 25°C and atmospheric pressure, Geochem. Cosmochim. Acta 44 (1) (1980) 85–94, https://doi.org/10.1016/0016-7037(80)90178-7.

[93] C.M. Miller, R.L. Valentine, Mechanistic studies of surface catalyzed H2O2 decomposition and contaminant degradation in the presence of sand, Water Res. 33 (12) (1999) 2805–2816, https://doi.org/10.1016/S0043-1354(98)00500-4.

[94] H. Aguiar, J. Serra, P. González, B. León, Structural study of sol–gel silicate glasses by IR and Raman spectroscopies, J. Non-Cryst. Solids 355 (8) (2009) 475–480, https://doi.org/10.1016/j.jnoncrysol.2009.01.010.

[95] I. Notingher, J.R. Jones, S. Verrier, I. Bisson, P. Embanga, P. Edwards, J.M. Polak, L.L. Hench, Application of FTIR and Raman spectroscopy to characterisation of bioactive materials and living cells, Spectroscopy 17 (2–3) (2003) 275–288, https://doi.org/10.1155/2003/893584.